Simulation studies of a novel scintillator detector with SiPM readout for muons of cosmic ray air showers

von

Marcus Wirtz

Bachelorarbeit in Physik

vorgelegt der

Fakultät für Mathematik, Informatik und Naturwissenschaften

RWTH Aachen

angefertigt am

III. Physikalischen Institut A

vorgelegt im **September 2014**

Erstgutachter und Betreuer

Prof. Dr. Thomas Hebbeker
III. Physikalisches Institut A
RWTH Aachen University

Zweitgutachter

Prof. Dr. Martin Erdmann
III. Physikalisches Institut A
RWTH Aachen University

Contents

1 Introduction

Mankind has been fascinated by the mysteries and the endless vastness of the universe for thousands of years. Questions about planetary movement, genesis of stars, cosmic background radiation and numerous other have concerned generations of physicists.
In August 1912, the field of research was expanded by a discovery of Victor Hess. Measurements of the electrical conductivity as a function of the altitude during a balloon ride in heights of up to 5000 meters led him to the assumption of high energy particles coming from space [1]. These particles, which continuously penetrate the atmosphere, are known today as cosmic rays. As a result of this discovery considerable efforts were made to learn about the origin of these particles.

These efforts are still made today. In order to learn about the origin of cosmic rays at the highest energy levels, scientists at the Pierre Auger Observatory, the world's largest detector field for the measurement of cosmic rays, plan to install a supplementary detector for measuring the muonic component of extensive air showers. As of today, there are several proposals but the final decision for one of these concepts has not yet been made. This work is introducing a novel detector, the Aachen Muon Detector (AMD), which has been developed at the RWTH Aachen University in order to meet the requirements of muon measurements.

In this context, the focus of this work is on simulation studies to analyse and improve the performance of the detector regarding the detection of single incoming muons. The first chapters will give a brief overview about cosmic rays and the resulting extensive air showers with a focus on the muonic component and the information it contains about the chemical composition of the primary particle. Afterwards an introduction of the Pierre Auger Observatory and the AMD is given. The latter one contains both the setup of the AMD and a description of the particle detection mechanism for this kind of detector.
The simulation studies in chapter 6 include three main goals. The first objective is to estimate the voltage signal caused by noise phenomena of silcon photomultipliers and a comparison to the signal of traversing muons. Second, simulations are performed to determine the optimal geometry setup of the AMD for the detection of muons. Finally, the performance of the system of optical fibers used in the detector for the transport of photons is investigated by studying two different options of fiber configurations: the singleclad and the multiclad fiber.

2 Cosmic rays

The energy spectrum of cosmic rays declines with higher energy and can be described as an exponential function of the form $F(E) \propto E^{-\gamma}$. The spectral index γ changes with energy, dividing figure 2.1 into four parts. The first part, the lower energy region up to $E \approx 5 \cdot 10^{15}\,\mathrm{eV}$ shows a spectral index of $\gamma \approx 2.7$. The following region shows a spectral index of $\gamma \approx 3.0$ and is confined from the first part by the *knee*. At energy levels of $E \approx 10^{17}\,\mathrm{eV}$ their exists a *second knee* which introduces a spectral index of $\gamma \approx 3.1$. Measurements of cosmic rays with energy levels around $E \approx 10^{18.5}\,\mathrm{eV}$ indicate another change of the spectral index, which is known as the *ankle*. Above energies of $E \approx 10^{20}\,\mathrm{eV}$ there is a *cutoff*, at which no particles can be measured anymore (cf. figure 2.1).

Numerous explanations for the measured energy spectrum are currently discussed in literature and multiple different accelerations mechanisms for cosmic rays are assumed. Suggested origins are supernova shock waves, gamma ray bursts, active galactic nuclei and black holes [2],[3].

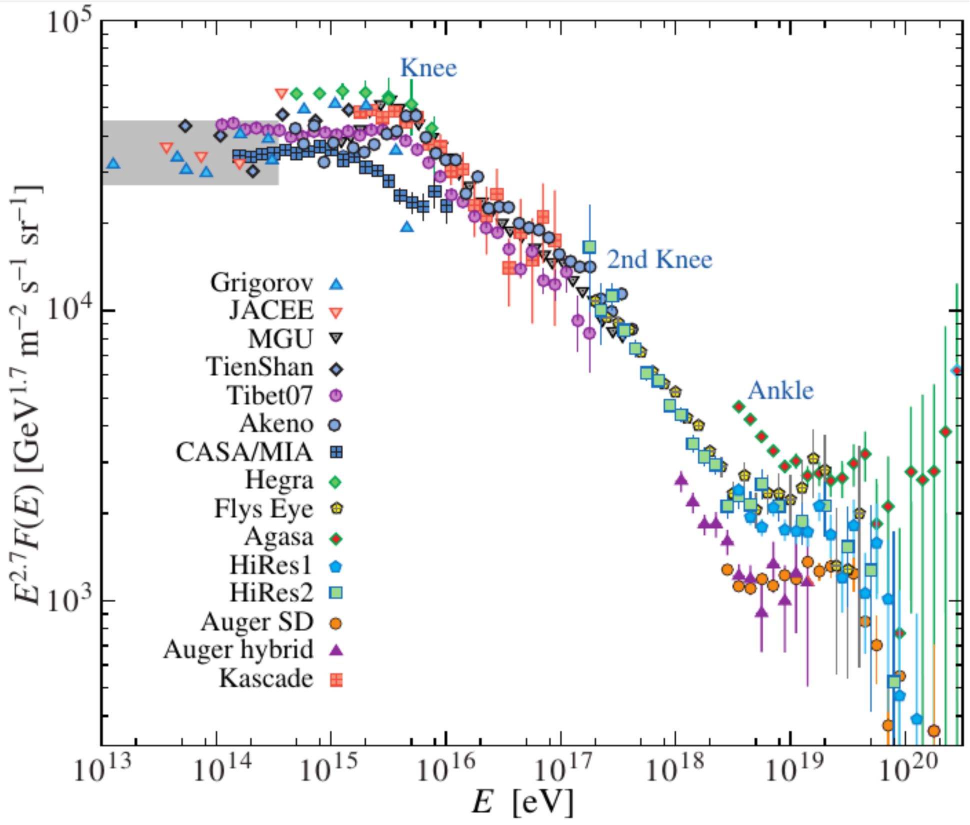

Figure 2.1: Energy spectrum of cosmic rays, reconstructed from air showers in several experiments. The spectrum is multiplied with $E^{2.7}$ to point out the structure within the data points. The grey rectangular highlights data from direct measurements [4].

The atomic nuclei with energies up to $E \approx 10^{15}$ eV can be measured directly by telescopes in the orbit and their chemical composition are therefore well known. However, since the flux density of cosmic rays declines with higher energy,the frequency of ultra high energy cosmic rays (UHECR) penetrating the atmosphere is rather small. UHECRs are cosmic rays with energies above 10^{18} eV. On average, there is a single particle per square kilometer per century and per steradian for an energy of 10^{20} eV [4]. Even a detector with the dimensions of a football field covering a hemisphere the solid angle of a hemisphere would detect only one of these particles every $\sim$ 1.600 years! These conditions combined with the fact that large statistics are needed for an exact analysis of cosmic rays lead to the conclusion that any kind of direct measurement is impossible. As a result the UHECRs have to be detected indirectly by the air showers they cause in the atmosphere.

As stated above, learning more about the origin of the UHECRs means dealing with the observation of extensive air showers (EAS). There are three fundamental properties of the primary particle, which are of particular interest: the arrival direction, the energy and the chemical compound. Especially the latter is very difficult to analyse, since there is no direct access to the primary particle [5]. In this regard, the next chapter illustrates a possibility to estimate the mass of the primary particle using the muonic component of extensive air showers.

3 Extensive air showers

The composition of the primary particle in cosmic rays up to energies of $E \approx 10^{14}\,\mathrm{eV}$ is approximately independent from energy. They are composed of $\sim 95\%$ protons, $\sim 4.5\%$ helium and $\sim 0.5\%$ heavier nuclei [6]. The chemical composition for the UHECRs is still unknown and an essential part of current research. If such a particle impacts the upper atmosphere, it interacts with molecules of the air and creates hundreds to billions of secondary particles, which is referred to as extensive air shower (EAS).

To examine an EAS more quantitatively, it is necessary to consider that the density of the atmosphere drops with increasing altitude according to the barometric formula

$$\rho(h) = \rho_0 \cdot e^{-h/h_0}, \qquad h_0 = \frac{p_0}{\rho_0 g} \quad , \tag{3.1}$$

where $\rho(h)$ is the density at the altitude h, $\rho_0 \approx 1.3\,\mathrm{kg\,m^{-3}}$ the density on sea level, $p_0 = 1\,\mathrm{bar}$ the atmospheric pressure, $g \approx 9.81\,\mathrm{m\,s^{-2}}$ the gravitational acceleration at the Earth and h_0 a characteristical altitude as defined in equation (3.1). It is very useful to introduce the *atmospheric depth* $X(h)$, which is defined as the integrated density over the altitude from infinity down to h (cf. equation (3.2)). Thereby, the atmospheric depth is a measure for the passed matter:

$$X(h) = \int_h^\infty \rho(h')dh' = \rho_0 h_0 \cdot e^{-h/h_0} \approx 1020\,\mathrm{g\,cm^{-2}} \cdot e^{-h/h_0} \quad . \tag{3.2}$$

For declined air showers equation (3.2) has to be multiplied by $1/\cos(\theta)$, recognising the fact that the shower has to pass more air.

The longitudinal development of an air shower can be described with a simple model, referred to as *Heitler model.* The cascade is described by a pure electromagnetic component. An incoming photon with energy E_0 produces an electron-positron-pair while the electrons and positrons can create a bremsstrahlung photon in turn. The mean free path λ of the particles depends on the density of air and hence on the altitude due to the changing density, but can be expressed by a constant step length X_{step}, since the atmospheric depth is defined.
In the Heitler model each particle will create exactly two new particles after passing a distance of X_{step}. The number of particles will be $N = 2^n$ after n steps (cf. figure 3.1). Another assumption made in this model is that the new particles equally share half of the energy of the mother particle. Thus, the energy after n steps is given by $E = E_0/N = E_0/2^n$. This process will continue until the point where the particles reach the critical energy E_C. At this energy the ionization effect overcomes the effect of bremsstrahlung, meaning the shower reaches its maximum and will die out [7]. Solving the equations $E_C = E_0/2^{n_\mathrm{max}}$

and $X_{\max} = n_{\max} \cdot X_{\text{step}}$ for the shower maximum $X_{\max}$ gives:

$$X_{\max} = X_{\text{step}} \cdot \log_2 \left(\frac{E_0}{E_C} \right) \quad . \tag{3.3}$$

In spite of the strong simplifications, the Heitler model results in a rather good estimation for the shower maximum.

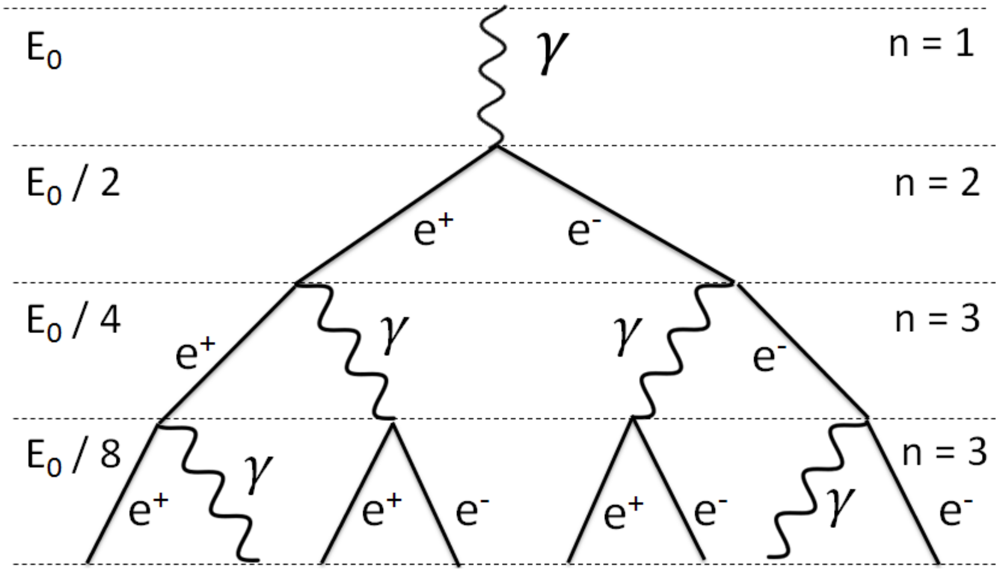

Figure 3.1: Schematic of an electromagnetic cascade in Heitler's model. A single photon of the energy E_0 splits up in an electron-proton-pair and starts the shower. Adapted from [7].

3.1 Components of an EAS

The processes which take place in a hadronic air shower are much more complex. When a primary particle of the cosmic rays penetrates the upper atmosphere it will hit a molecule's nucleus. In this collision various nucleus fragments, like mesons (π,K,...) and other hadrons (p,n,...), are generated (cf. figure 3.2). These fragments, building the **hadronic component** of the EAS, collide with more air molecules or decay.

The produced neutral pions have a rather short life time ($\tau_{\pi^0} \approx 8 \cdot 10^{-17} s$) [8]. This means that approximately 30% of the pions decay in two photons in the process $\pi^0 \rightarrow \gamma + \gamma$ (Γ = 98.8%, indicates the probability of this decay mode) [8], since the charged and uncharged pions (π^0,π^+,π^-) are produced in equal frequencies [9]. This decay is the leading cause for the development of the **electromagnetic component**. A smaller portion of the electromagnetic component comes from a muon decay $\mu^- \rightarrow e^- + \nu_\mu + \bar{\nu_e}$. Particulary the electrons and positrons of the electromagnetic component excite molecules like nitrogen in the atmosphere. The resulting fluorescence light by the following deexication can be used to obtain a calorimetric measurement of the shower.

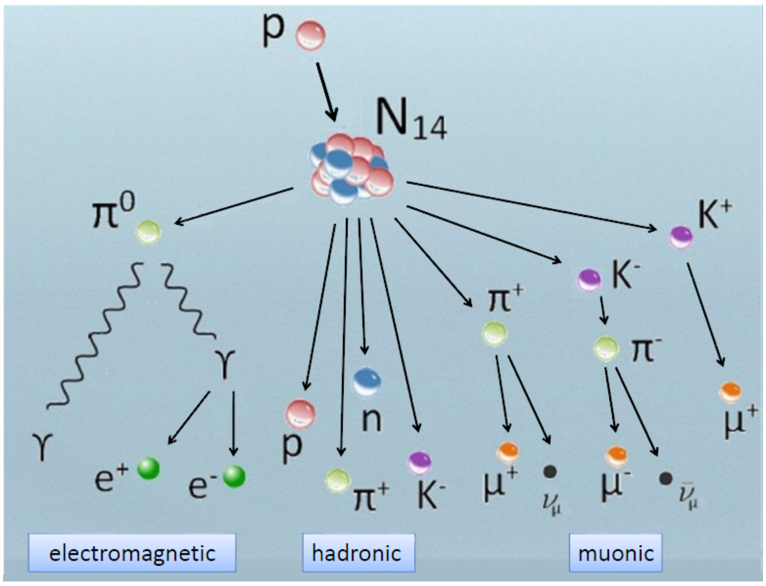

Figure 3.2: A sketch of some possible interactions which lead to the hadronic, electromagnetic and muonic component of an air shower.

As shown in figure 3.3, the number of mesons reachs a maximum at an atmospheric depth of $X \approx 500\,\mathrm{g\,cm^{-2}}$ and drops rapidly from this point on due to the decays of the kaons and pions. The kaons decay with a lifetime of $\tau_K \approx 10^{-8}\,\mathrm{s}$ to muons $K^{\pm} \rightarrow \mu^{\pm} + \nu$ $(\Gamma = 63.5\%)$ and to pions $K^{\pm} \rightarrow \pi^{\pm} + \pi^{0}$ $(\Gamma = 20.7\%)$, where ν indicates the corresponding neutrino. The charged pions decay with a lifetime of $\tau_\mu \approx 3 \cdot 10^{-8} s$ into muons $\pi^{\pm} \rightarrow \mu^{\pm} + \nu$ $(\Gamma = 99.99\%)$ [8]. In short, the mesons cause the **muonic component** of the EAS. Except for the small proportion of the muons which decay to electrons and positrons, the muons reach the ground in large numbers since they are much less influenced by bremsstrahlung and multiple scattering due to their higher masses.

Since the fraction of highly boosted muons decaying during the time of flight is small, the number of muons becomes constant when the meson fraction drops (cf. Fig 3.3). At this plateau, the muon fraction reaches a value of approximately 10%. Since the muons are produced in mesonic decays, their total number is an indicator for the total number of hadronic interactions which, in turn, depends on the number of hadrons in the primary particle. This fact makes the properties of the muonic component sensitive to the mass of the primary particle [10].

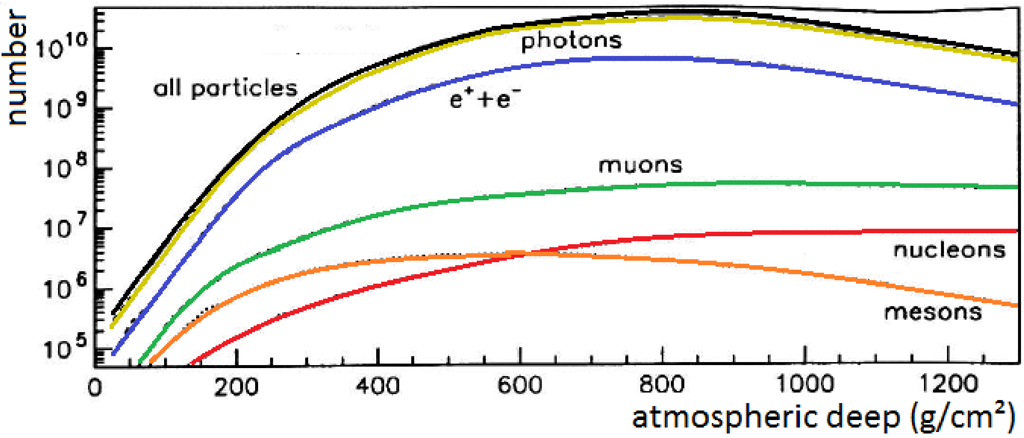

Figure 3.3: The typical longitudinal profile of an EAS with a particle energy of $E_0 \approx 10^{18}$ eV. Presented is the total number of particles as a function of the atmospheric depth. Adapted from [11].

3.2 Atmospheric production depth of muons

As recent surveys show, especially the muon production depth (MPD) contain information about the nature of the primary particle [5]. The arrival time of muons on the ground allows inferences to their production height z, assuming some approximations: the muons are produced along the shower axis and are travelling straight-lined with the speed of light. The muon reachs the ground at a position

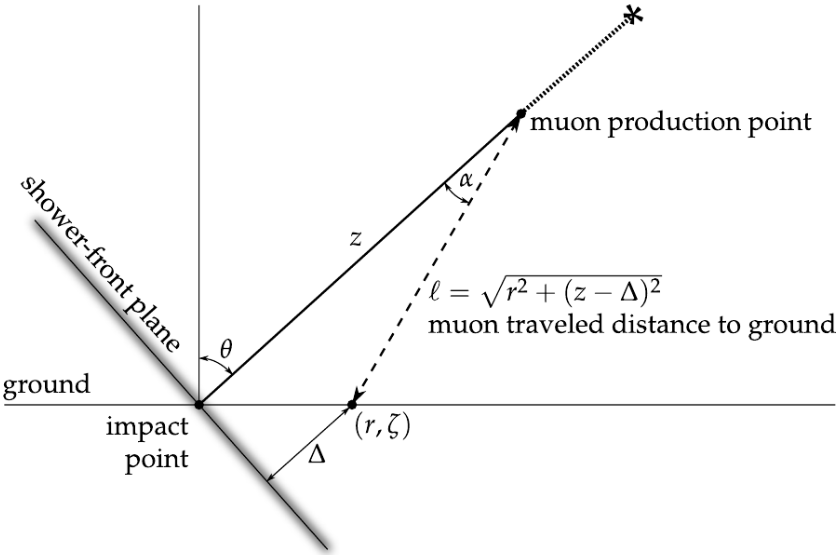

Figure 3.4: Reconstructed production height z of muons in air showers. The trajectory of the muon is assumed as a straight line, such that the travelled distance l can be calculated geometrically. Taken from [5].

which is defined by the radius r from the impact point and the azimuth angle ζ (cf. figure 3.4) after a travelled distance of

$$l = \sqrt{r^2 + (z - \Delta(r,\zeta,\theta))^2} = c \cdot t_g \quad . \tag{3.4}$$

Δ is thereby the distance from the ground impact point to the shower plane as can be seen in figure 3.4. Unfortunately, the delay of the muons is not solely determined by the different geometrical distances, but is also caused by a kinematic delay t_ϵ which originates from inelastic collisions with atomic electrons [5]. Therefore, the measured time is $t = t_g + t_\epsilon$. Furthermore, the production point of muons is not exactly on the shower axis, caused by the additional length $\langle z_\pi \rangle$ which the pion travels before the decay. These effects leads to a modification of the mapping between the arrival times and the production height:

$$z \approx \frac{1}{2}\left(\frac{r^2}{c(t - \langle t_\epsilon \rangle)} - c(t - \langle t_\epsilon \rangle\right) + \Delta(r,\zeta,\theta) - \langle z_\pi \rangle \quad . \tag{3.5}$$

The corresponding atmospheric depth X^μ of the muons can be calculated with equation (3.2). A distribution of the average MPD (X^μ_{max}) for different events with protons and iron nuclei as primary particles can be seen in figure 3.5.

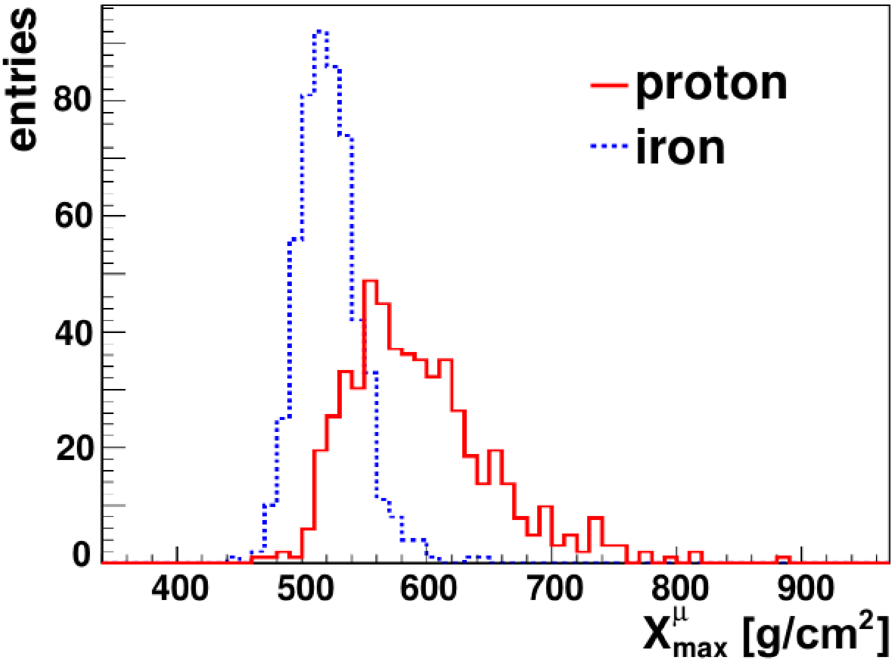

Figure 3.5: A distribution of the muon production depth (MPD) for protons and iron nuclei based on air shower simulations with an energy of 30 EeV and with zenith angles between 55° and 65° including the hadronic interaction model. The mean and the variance of the distributions show a clear dependence on the mass of the primary particle. Taken from [5].

It is based on simulated showers with energy $E = 30\,\mathrm{EeV}$ and incidence angles between $\Theta = 55°$ and $\Theta = 65°$. The chosen hadronic interaction model is EPOS-LHC and the MPD is reconstructed according to equation (3.4). The distribution of the MPD varies as a function of the mass number of the primary particle. The mean as well as the variance of the distibution declines with heavier elements [5]. Thus, the measurement of muons will be an important element for ground based detector fields because they are a good indicator towards the identify of the primary particle.

4 The Pierre Auger Observatory

The Pierre Auger Observatory is located in the Pampa Amarilla, Argentina, near the city Malargüe. The observatory, which is the largest of its kind is studying ultra high energy cosmic rays by the extensive air showers produced by them in the atmosphere.
The selection of the location is anything but coincidence. Several conditions make this Pampa an ideal location: the place is situated 1400 m above sea level according to an atmospheric depth of $X_0 = 875\,\mathrm{g\,cm^{-2}}$, whereby the distance to the shower maximum is reduced. This is necessary in order for the fluorescence light yield to be as high as possible. A further advantage is the natural protection against cloudy weather provided by the Andes. The landform is rather flat, which is necessary to reconstruct the incidence angle of the shower as good as possible.
The observatory combines two independent methods of detection into one hybrid-detector. This allows an improvement of the energy and angular resolution and therefore a more accurate measurement of the shower.

4.1 Surface detector

The surface detector (SD) is the main part of the Pierre Auger Observatory and is composed of over 1600 tanks, filled with $12\,\mathrm{m}^3$ pure water. They are placed in a hexagonal array with a distance of 1.5 km each, covering a total area of $3000\,\mathrm{km}^2$.

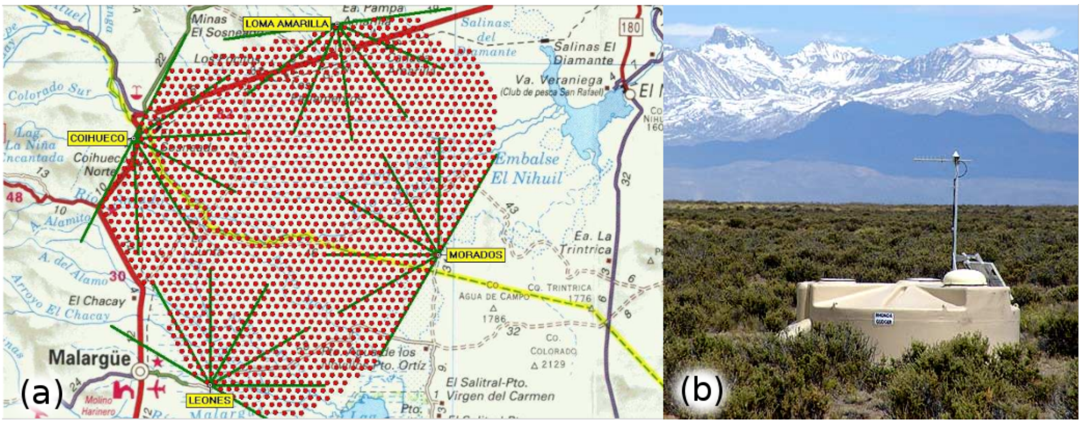

Figure 4.1: (a) Map of the Pierre Auger Observatory. The red dots represent the 1600 SD stations. The opening angles of the 24 fluorescence telescopes are shown by green lines. [9] (b) Closeup view of a water Cherenkov SD tank [12].

The tanks are fully lightproof. Thus, having a light pulse inside the tank means a traversing charged particle which speed is faster than the speed of light in water. This Cherenkov light will be detected by three photomultiplier tubes watching the water from inside the tank. The shower front of an EAS will generate light in several tanks within a very short period of time. The information is send via cell phone technology to the main station. Up to 30 stations can be triggered by an extensive air shower of 10^{19} eV under ideal conditions [13].
To calculate the incidence angle of the shower front, the mean arrival times of the traversing particles are measured. Assuming a particular shape of the shower front (the simplest is a plane), one can use the mean arrival times of each triggered SD tank to derive the incidence angle by a geometrical calculation. In a real air shower event this leads to an angular resolution of 1.1° or better [13].

4.2 Fluorescence detector

The SD is supplemented by the fluorescence detector (FD). It is comprised of 4 stations, the 'eyes', which are surrounding the surface detector area and overseeing the atmosphere above this area. Each eye consists of six fluorescence telescopes where a camera built out of photomultiplier tubes detects the fluorescence light generated by the electromagnetic component of the shower. The incoming light is focused by a spherical mirror with a diameter of 3.6 m onto the sensitive area of the camera [14]. Except for a shutter, the whole aperture is built in a housing to minimize interfering light from the surrounding. In addition, the housing provides a temperature control and a protection against dust. Each eye covers a wide field of view of 30° in azimuth and 28.1° in elevation direction [15]. A schematic view of the FD is given in figure 4.2.

Since a single ionizing particle can produce up to ~ 5 fluorescence photons per m, the 440 camera pixels in the fluorescence telescopes afford a mapping of the shower core. The FD therefore allows to track the longitudinal development of the shower. Through a linear regression of this trace the shower detector plane (SDP) is fixed (cf. figure 4.3). While the charged particles moves along the shower core, the fluorescence light is produced at different times. Therefore, the angle χ_0 and the perpendicular distance R_p is fixed by measuring the different arrival times of the incoming fluorescence light as indicated in figure 4.3. The energy can also be estimated with the help of the FD measuring the energy which is deposited into fluorescence light. This allows an energy resolution with a systematic uncertainty of 14% [5]. The ability to measure the energy can be gradually adapted by the surface detector using hybrid events, since the reconstructed signal in a distance of 1000 m from the shower core shows a dependency on the energy. This adaption significantly improves the uncertainties of the energy measurement for the SD [16].

A big challenge concerning the FD is the very limited duty cycle: due to the requirement good weather and absolute darkness in the night for FD measurements, as the fluorescence light is very faint, the overall duty cycle of the FD is only around 10% compared to the 100% duty cylce of the SD [13].

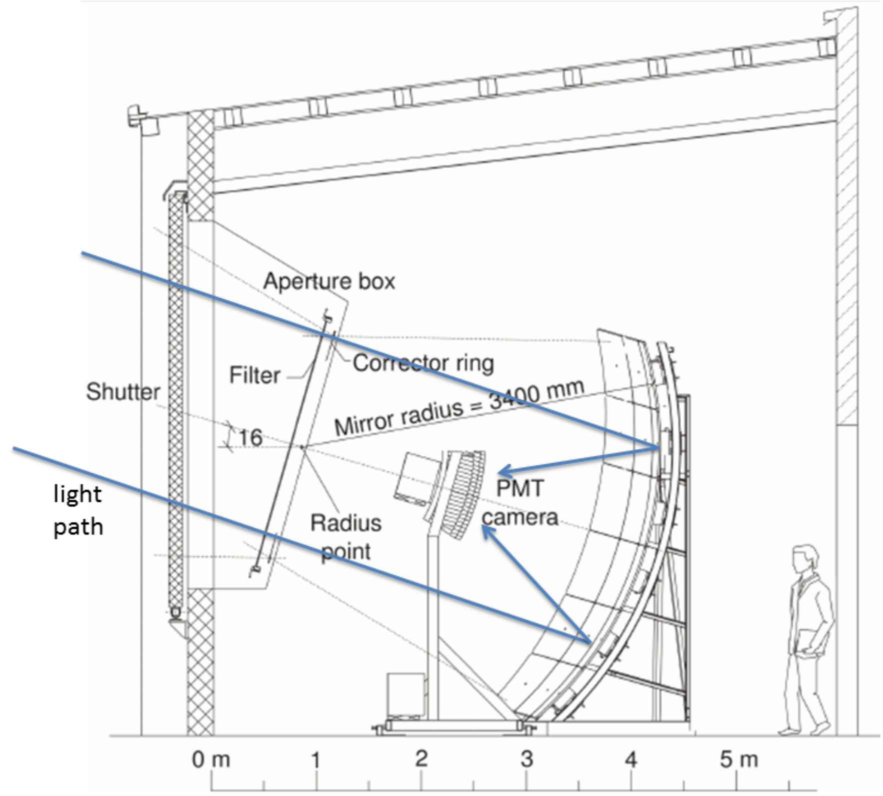

Figure 4.2: Schematic of one telescope of the fluorescence detector. The incoming light is focused by the spherical mirror and is detected by the photomultiplier tubes (PMT) at the camera. To minimize light from the surrounding, the whole relescope is encircled by a steel construction. Adapted from [13].

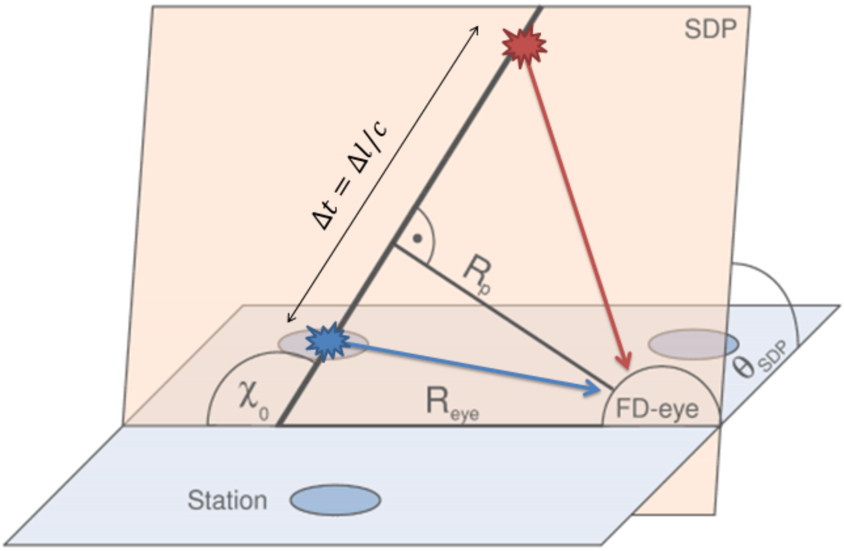

Figure 4.3: Reconstruction of the showers incidence angle χ_0. R_p is the perpendicular distance between the detector and the shower core, R_eye the distance between the detector and the ground position of the shower core and θ_SDP the angle between the shower detector plane and the ground plane. The red arrow represents early produced fluorescence light and the blue arrow fluorescence light produced during the shower development after the time Δt [17].

4.3 Auger update program 2015

Recently, the Pierre Auger Collabaration decided to update the Pierre Auger Observatory for several reasons. Two of their objectives for this upcoming update program are formulated as the followings [18]:

- *"elucidate the origin of the flux suppression at the highest energies"*
- *"measure the composition of UHECRs up to highest energies, with sufficient resolution to detect a 10% proton component"*

For this purpose, different proposals of muon detectors compete for the supplement of the SD. Some of them share the electronics of the SD-tank. The proposals are either placed below or above the tank or below the surface of the Earth in a distance to the SD-tank [19],[20]. The Aachen Muon Detector (AMD) is a proposal for a detector which is placed below the SD tank and is based on silicon photomultiplier (SiPM) detection.

5 Aachen Muon Detector

The Aachen Muon Detector (AMD) is a proposal for the update program of the Pierre Auger Observatory and is developed at the RWTH Aachen University at the III. Physikalisches Institut A. The AMD is planned to be installed directly below the SD tank. This provide some advantages: the water tank is used as a shielding against the electromagnetic particles of the air shower which are the main background for the AMD. The power supply for the electronics can be shared with the SD tank. In addition, the trigger system of AMD can be improved by the data of the SD and a direct comparison of both responses is possible. Since the AMD is a silicon photomultiplier (SiPM) based detector, the next chapter provides a short overview about the basic characteristics of SiPMs.

5.1 Silicon photomultipliers

SiPMs are a relatively young technology and promising devices for the detection of light. It is a semiconductor component (cf. Fig. 5.1(a)) composed of an array of avalanche photodiodes (APDs). A single SiPM is very compact and has a sensitive area of few mm^2, featuring the substructure of the APDs (cf. Fig. 5.1(b)).

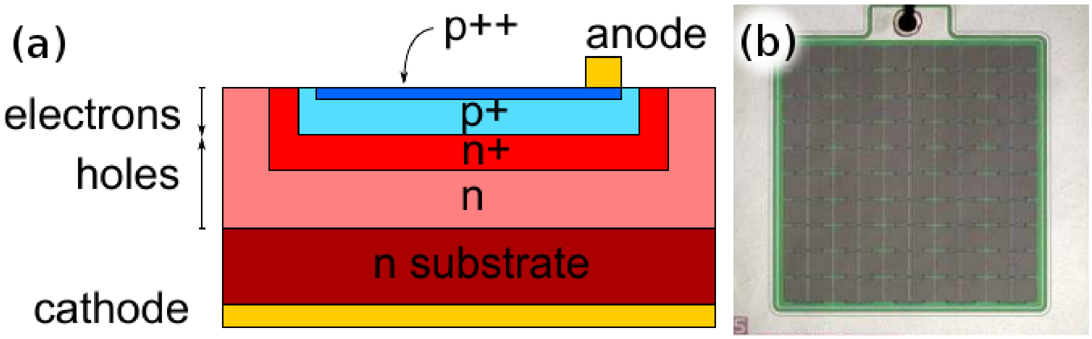

Figure 5.1: (a) Schematic structure of a single photodiode with the different layers of the semiconductor. Adapted from [21]. (b) Photograph of a SiPM chip with an area of 1 mm^2 and 100 APDs. The space between the photodiodes is not sensitive [22].

They have several advantages over conventional, commonly used photomultiplier tubes (PMTs) like their small size, their immunity to powerful magnetic fields and the promising high photon detection efficiency shown by several SiPM prototypes. Furthermore, SiPMs do not need such high voltages as PMTs, SiPMs are operated with a moderate voltage of 30-150 V compared to $\sim$ kV for PMTs.

The SiPMs are operated as the following: In the p-n-junctions a depletion zone is formed by applying a reverse bias voltage V_{bias} to the SiPM. If an incoming photon hits the depletion zone of one cell, it can creates an electron-hole pair. The charged carriers are accelerated in the pn-junction of the semiconductor and create new electron-hole pairs. This causes an avalanche of charge carriers as the APDs in the SiPM are operated in Geiger-mode. Therefore, there is a maximal amplification and the output signal is equally high, one photon equivalent (p.e.), for each detected photon. As the APDs of the SiPM are operated in Geiger-mode, the avalanche would be self-sustaining and the APD would be damaged thermally. Thus, one quenching resistor has to be connected in serial to each APD of the SiPM. This additional resistor stops the process as the increasing current during the avalanche causes an increasing voltage at the resistor. Thereby, the voltage at the APD decreases until the APD reaches its initial state.

A disadvantage of an SiPM is the strong dependency of the operating temperature, which is very well studied in the meantime.
However, there are some false signals due to **noise phenomena**. The thermal noise is omnipresent with a mean noise rate of $f_{th} \approx 100\,\mathrm{kHz\,mm^{-2}}$. It results from the thermal production of electron-hole pairs, which can lead to an avalanche. Another noise effect is the optical cross-talk, whereby the photon also recombines with a neighbouring cell so that an additional electron-hole pair is created. The third important phenomenon is the after pulse, where electrons of the previous avalanche, captured by imperfections in the silicon lattice, can cause a new avalanche while they are released again.
These correlated noise effects can be studied in detail by dark count measurements. Therefore, the SiPM has to be operated in total darkness. The resulting number of cell breakdowns refers then to the dark noise of the SiPM [15].

5.2 Baseline design

A construction of 12 steel I-beams and two 5 mm thick steel plates compose the housing of AMD. The total dimensions of this support structure is approximately 4 m x 3.6 m x 10 cm. The space between the steel I-Beams provides shelves for eight trays with a length of 3.6 m each. The trays in turn, provide 8 shelves for the scintillating tiles, so that there are 64 tiles in total (cf. figure 5.2). The whole setup is highly modular and rarely needs maintenance, since the components are very robust and there are no consumables. In contrast to the fluorescence detector, the AMD is able to work permanently at all times and all weather conditions leading to a 100% duty cycle.
Each tile is readout through an SiPM sitting on one side of the tray, so that there are in total 64 SiPMs. A traversing particle produces light in the scintillating tiles which is led to the SiPMs through a system of two optical fibers per

tile.

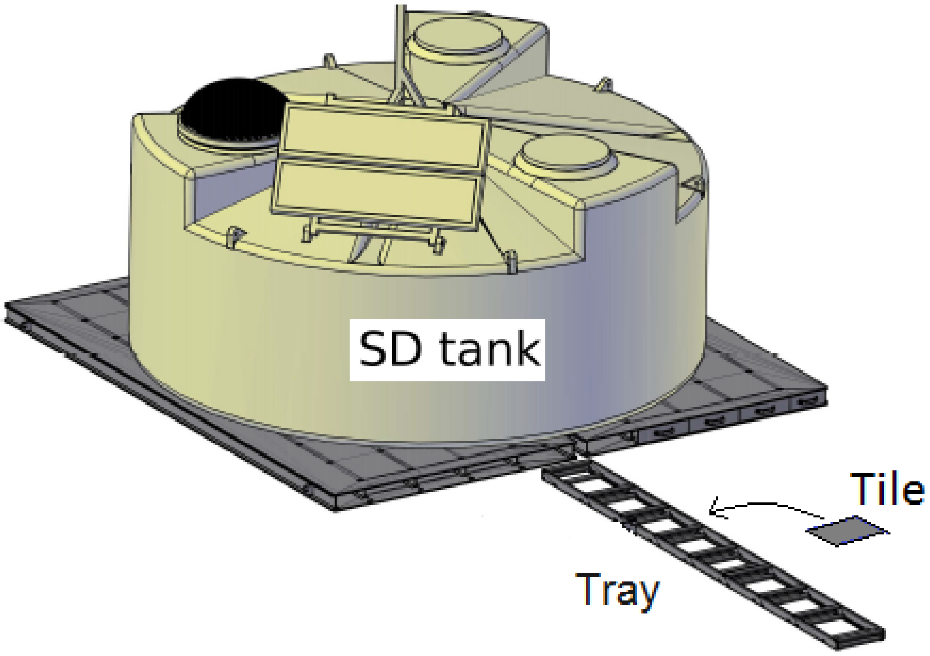

Figure 5.2: Setup of the AMD. The SD tank is placed on a steel support structure, containing 8 trays with 8 scintillating tiles each.

5.2.1 Scintillating tiles

The purpose of the scintillating tile shall be the production of photons, if a charged particle is crossing its BC-408 scintillator material. The produced photons are emitted isotropic and have a mean wavelength of $\lambda = 430\,\mathrm{nm}$ in the case of BC-408 scintillator [23]. The selection of the pitch size d for the scintillating tile is still not decided for the AMD. First of all, the size is limited by the demand of the steel support, since they have to fit into the shelves between the I-beams. For the case of 8 shelves between the I-beams, the maximum tile-size is limited to 360 mm. In principle, there is no lower limit for the tile-size, but there improves when increasing the tile-size d:

$$\sigma_{\mathrm{x}} = \frac{d}{\sqrt{12}} \tag{5.1}$$

For the subsequent simulations tile-sizes between 260 mm and 360 mm will be analysed, to find the size with the best performance for the triggering of muons.

5.2.2 Optical fibers

To transport the produced light in the scintillating tile to the SiPM readout there is a system of two optical fibers.
In the scintillating material of the tiles a groove is milled to house a curved wavelength shifting fiber (WLS) of 1 mm diameter, the 'sigma fiber', which has its name due to its shape (cf. figure 5.3). The WLS is glued into the groove with a glue whose refractive index should be similar to the refractive index of the scintillating tile to minimize surface effects. The side of the fiber ending in the scintillating tile is mirrored to minimize photon losses. There are two parameters which characterise the course of the sigma fiber within the tile. The padding p describes the distance of the sigma fiber to the edge of the tile and the radius r describes the curved radius of the fiber (cf. figure 5.3). The sigma fiber and the tile together are surrounded by a thin aluminium foil, which makes the tiles extra tight against light in addition to the surrounding steel construction. Also, the aluminium foil reflects the produced light in the tile back into the scintillating material to increase the chance that the light enters the WLS fiber.

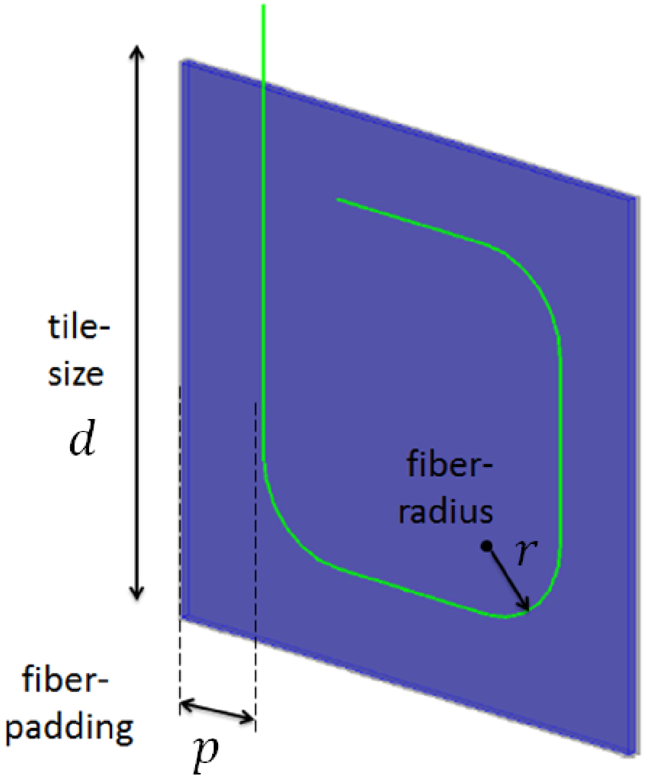

Figure 5.3: The sigma fiber lays inside a groove, which is milled in the scintillating tile. The tile-size d refers to the pitch size of the tile, the fiber padding p to the the distance between the straight pieces of the sigma fiber and the edge of the tile and the fiber-radius r to the curved radius of the sigma-fiber. Adapted from [24].

The sigma fiber is connected with a straight optical fiber (waveguide), which transports the light to the end of the tray in a distance of 0.3 m - 2.9 m according to the tile position on the tray. At the end, each waveguide ends on the sensitive area of a 1 x 1 mm^2 SiPM. 32 Hamamatsu SiPMs on four trays share one EASIROC (Extended Analogue SI-pm ReadOut Chip) electronic board for the readout.

At present, there are two discussed options regarding the optical fibers: The BCF-92 (sigma fiber) and BCF-98 (waveguide) singleclad fiber, which are made of an cylindric polystyrene-based core with a refractive index of $n_{core} = 1.60$ and an acrylic cladding with a refractive index of $n_{clad,1} = 1.49$. The alternative is a BCF-92 and BCF-98 multiclad fiber with an additional cladding of fluor-acryl with a refractive index of $n_{clad,2} = 1.42$ [25].

5.2.3 EASIROC

The signal of the SiPMs is analysed by the EASIROC, standing for *Extended Analogue SI-pm ReadOut Chip*. The EASIROC is a low power front end chip which is dedicated to readout SiPM detectors.

The EASIROC board as used in the AMD is shown in figure 5.4. The field-programmable gate array (FPGA) is a programmable logic chip that is used for the steering of the EASIROC. It contains the trigger logic for air shower events

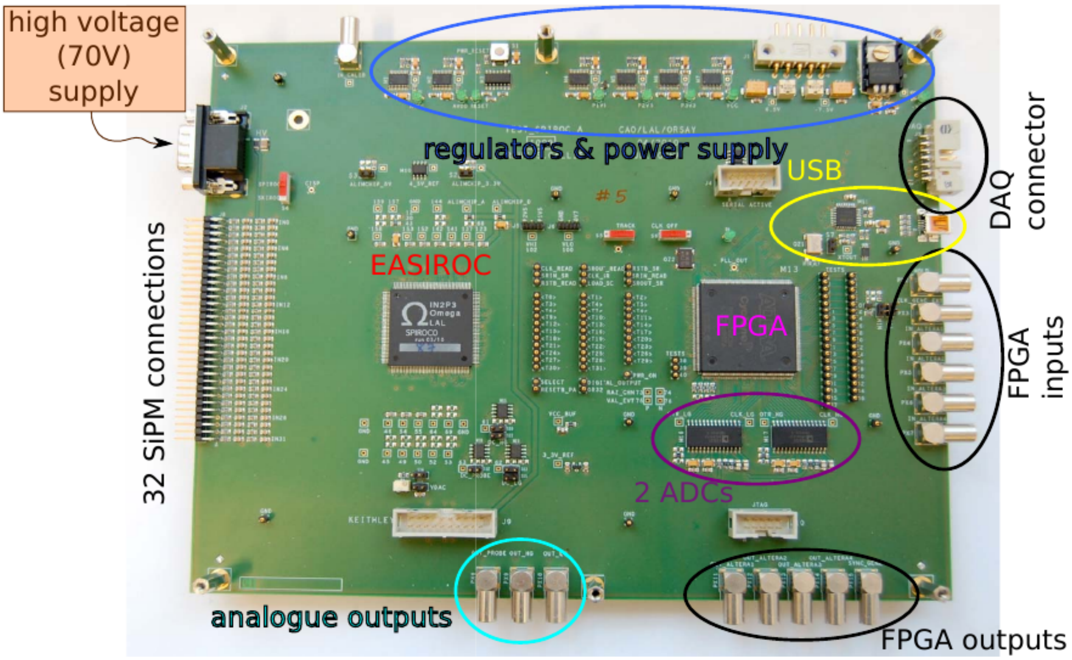

Figure 5.4: The EASIROC board as it will be used for the AMD. The FPGA is an integrated circuit and contains the trigger logic for the EASIROC. The EASIROC transforms the voltage trace of the SiPMs in an extended signal to decide if a trigger occured.

and buffers and relay data digitized by the EASIROC to the measurement computer.The EASIROC itself receives the voltage trace of the SiPMs. This voltage trace consists of very short pulses which have to be streched for evaluation, which is done by the slowshaper and the fastshaper. The discriminator in the EASIROC receives the shaped sigal (15 ns reaching time) of the fastshaper and the threshold which is set by an integrated 10-bit DAC and thus decides if a voltage signal is interpreted as trigger.

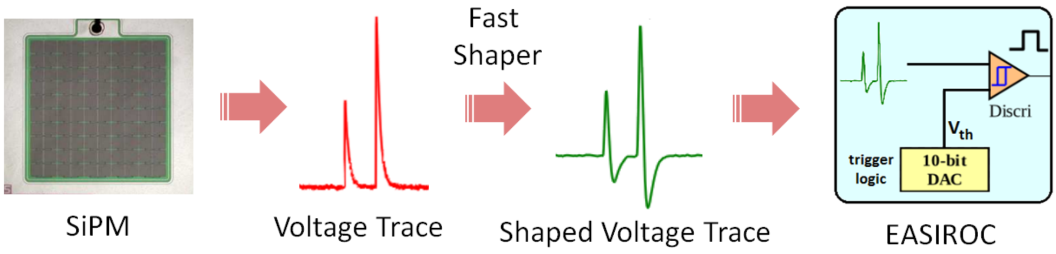

Figure 5.5: Schematic of the data processing. The voltage trace of the SiPM is streched by the slowshaper in the EASIROC and afterward analysed from the trigger system in the EASIROC.

Therefore, the fastshaper is of particular interest for this thesis, because it generates the pulse form for the trigger system and will be used in the following analysis to calculate the trigger efficiency and the *dark noise rejection*. Unfortunately, there is no possibility to measure this signal directly for the EASIROC, which is why the subsequent analysis is based on the time compressed pulseform of the slowshaper (cf. figure 6.2). The pulse form of both shapers are hopefully similar except for the pulse length.

5.3 Detection of charged particles

The plastic scintillator of the tiles is of the type BC-408 with a refractive index of $n = 1.58$. If an incoming charged particle, like a muon, traverses the scintillator it will excite the atoms of the scintillator. When the atoms move back to their ground state, they emit light. The total deposition of energy in the scintillator is subjected to statistical fluctuations. The distribution is very well described by a landau distribution [26]. In a first approximation the number of photons which reach the SiPM is also described by a landau function as can be seen in figure 6.12.

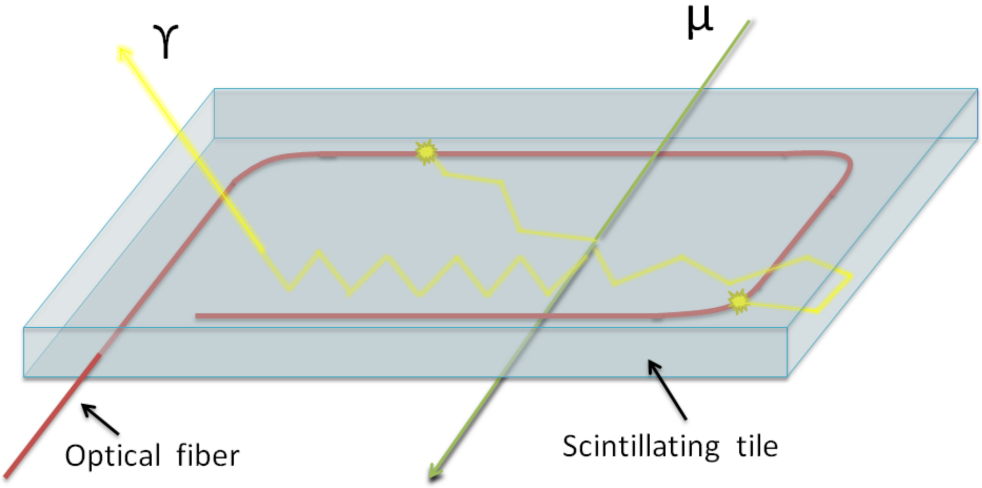

Figure 5.6: Sketch of the functional principle of a scintillating tile (blue) combined with the 'sigma fiber' (red). A single incoming muon (green) produces scintillating light (yellow) in the tile. The photons are reflected by the inner boundary of the scintillating tile as long as the incidence angle is high enough. The more reflections the higher the possibility for the photon to leave.

When a photon hits the inner boundary, it depends on the incidence angle wether the photon will be reflected or leave the tile. If the incidence angle (in relation to perpendicular) is less than $\Theta_C = \arcsin(1/1.58) \approx 39°$, the photon will leave the tile. To get transported to the SiPM, the photons have to enter the sigma fiber first (cf. figure 5.6). This means that they have to hit the WLS fiber at an incidence angle bigger than $\Theta_C = \arcsin(n_{clad}/1.58)$. A comparison between the refractive indices of the claddings points out that the probability of entering the fiber is smaller for the multiclad fiber. However, if the photons are inside the fiber it is more difficult for them to leave again. The fiber which show the best overall performance should be examined in the following simulations.

5.4 Implementation in Geant4

The simulations in this work are conducted using the Software 'GEANT 4' [27], a toolkit for the simulation of silicon photomultipliers [28] and mean values from simulations with 'CORSIKA' [29]. The transfer of the setup, as described above in the Geant4 system can be seen in figure 5.7.
The simulations are conducted for the SiPM-model 'Hamamatsu S12651-050' with a total area of 1 x 1 mm^2 consisting of an array of 400 photodiodes. This new SiPM-model has a reduced cross-talk probability in comparison to the model which had been installed in the AMD protoptype when the new model was not available yet [30]. The powerful toolkit already contains all noise phenomena as described above and transforms them together with the signal into a voltage trace. This voltage trace is shaped according to the EASIROC 'fastshaper' to read out the data. In this simulations the shaper is based on measurements [31] from the EASIROC output signal.

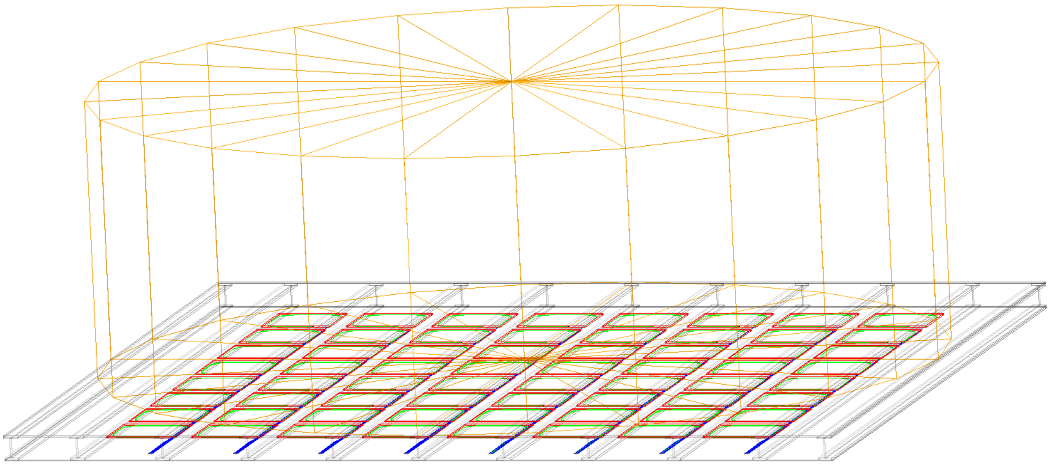

Figure 5.7: Screenshot of the AMD setup in Geant4. The water tank (yellow) shown is for illustration only and has no influence on the simulations. Shown are the 64 scintillating tiles (red), the sigma fiber (green), the waveguides (blue) and the steel support (grey). The SiPMs are sitting on the front ends of the waveguides.

6 Performance simulations for AMD

The results presented in this chapter are based on simulations with Geant4 as described above and single incoming particles, which are adapted to the properties of particles in a real air shower. The denoted energy intervals $E = [10^{\gamma_1}, 10^{\gamma_2}]$ MeV in the simulations refer to an uniform distribution of the exponents in the interval $[\gamma_1, \gamma_2]$. The angle intervals refers to a uniform distribution over the solid angle. For the optical fiber the multiclad fiber is used, which will be compared with the results of the singleclad fiber in section 6.8.

The main aim of theses simulations is to optimise the AMD to an optimal measurement of muons. A simple trigger is suggested which should maximise the efficiency for the triggering of muons on the one hand and minimise the noise level on the other hand. In a next step, this thesis figures out an optimised configuration of the geometry regarding the size of the scintillating tiles and the shape of the 'sigma fiber' (cf. figure 5.3). This optimised configuration is also characterised by the best possible efficiency for triggering an incoming muon. To estimate the influence of the dark noise of SiPMs on the signal by incoming muons, the next section presents the *dark noise rejection* of SiPMs.

6.1 Dark noise rejection

The relatively high noise rate is still a reason for critics to refuse the application of silicon photomultipliers.Therefore, this chapter estimates the number of events which are triggered by dark noise of the SiPM, using a toolkit for SiPM noise [28]. These results will be compared to the number of events triggered by muons later on in section 6.4. Therefore, a very simple criterion for the trigger is assumed: if the voltage trace after the EASIROC fastshaper exceeds a fixed voltage U_{thres}, an event is interpreted as triggered. In this context, the trigger threshold U_{thres} should be high enough that the dark noise is not able to exceed it. Otherwise, a trigger by a dark noise event would be interpreted as a traversing particle. To find this minimal threshold value, the *dark noise rejection* will be evaluated:
Since the front of air showers traverses a single station of AMD in the time interval of $\Delta t \approx 10\,\mu$s, the noise is simulated for this time window as well, as it can be seen in figure 6.1. This exemplary figure plots two 'normal' cell breakdowns by thermal noise and one event of two simultaneous breakdowns caused by the effect of cross-talk (cf. chapter 5.1). In this thesis the *dark noise rejection* will be defined as following:

$$\epsilon_{\text{noise}} = \frac{N_{\Delta\text{t}}(U_{\Delta\text{t}} < U_{\text{thres}})}{N_{\text{tot}}} \quad . \tag{6.1}$$

$N_{\Delta t}(U_{\Delta t} < U_{\text{thres}})$ is the part of noise simulations where the voltage of the shaped signal is smaller than the threshold voltage U_{thres} over the whole time windows Δt and N_{tot} is the total number of noise events. The simulations provide the voltage trace of the SiPM which has a very short temporal extension. It is possible to use only the maximal value of this voltage trace instead of the shaped voltage trace. However, this would disregard the overlap of two noise events which occure in a very short period of time, as it is the case for 'after pulsing' (cf. chapter 5.1). In this case, the amplitudes of the shaped signal by the EASIROC would add up to a higher value and could reach the next threshold voltage.

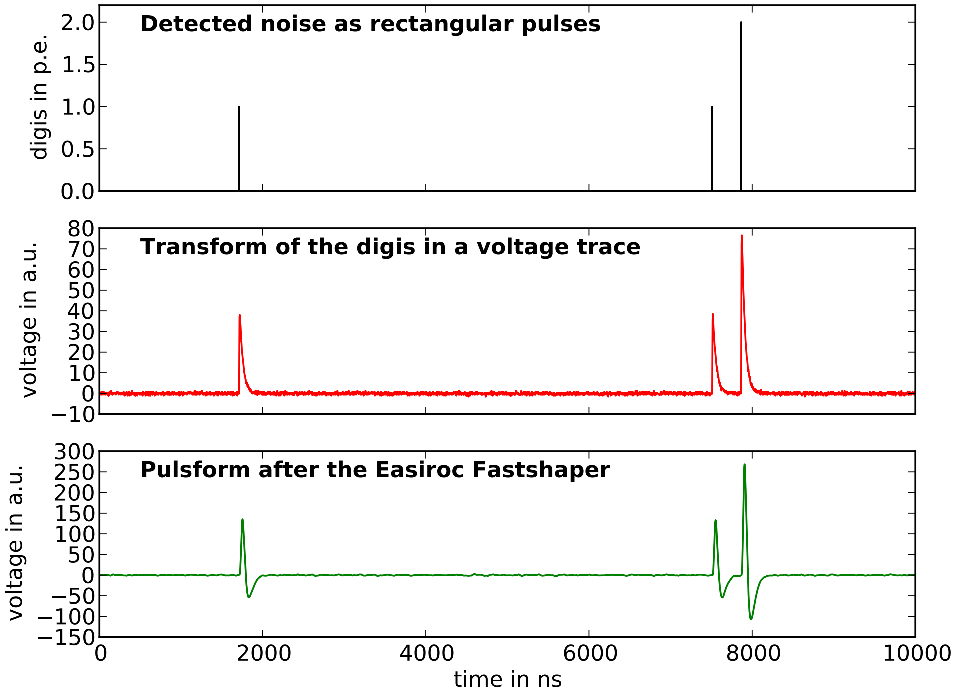

Figure 6.1: Simulated dark noise events of a Hamamatsu silicon photomultiplier of model S12651-050. The digis show chronologically the signals of cell breakdowns by thermal noise, optical cross-talk and after pulsing. The middle figure is the simulated resulting voltage trace of the SiPM and the figure on the bottom the signal from the EASIROC fastshaper.

The pulse form after the EASIROC fast shaper is calculated by a convolution of the SiPM voltage trace with the measured slow shaper response for a short input signal (cf. figure 6.2) in consideration of the shorter extension of the fast shaper signal. This calculation is only a first approximation, since the pulse form of the slow shaper and the fast shaper may differ.

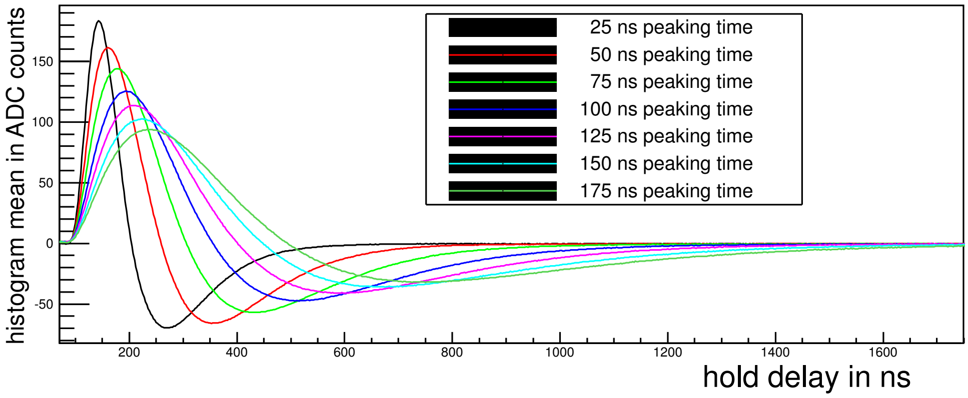

Figure 6.2: Measurements of the voltage signal of the EASIROC slow shaper for different peaking times. Taken from [31].

Since the shaper models the incoming signal according to its pulse form, the information about the voltage is only known up to a constant factor. To make use of this shaped signal, a calibration with the photon equivalents of the input signal has to be done. For this purpose, only isolated digis with a time difference to their neighbour peaks larger than 500 ns are considered. A linear relationship between these quantities is assumed:

$$U_{\text{shaped}} = m \cdot n_{\text{p.e.}} + b \quad , \tag{6.2}$$

where $n_{\text{p.e.}}$ is the number of photo equivalents and U_{shaped} the corresponding maximum voltage of the shaped signal. The linear regression for the mapping between photo equivalents and the amplitude of the shaped signal in arbitrary units is shown in figure 6.3. The uncertainties result are the result of the sample variance.

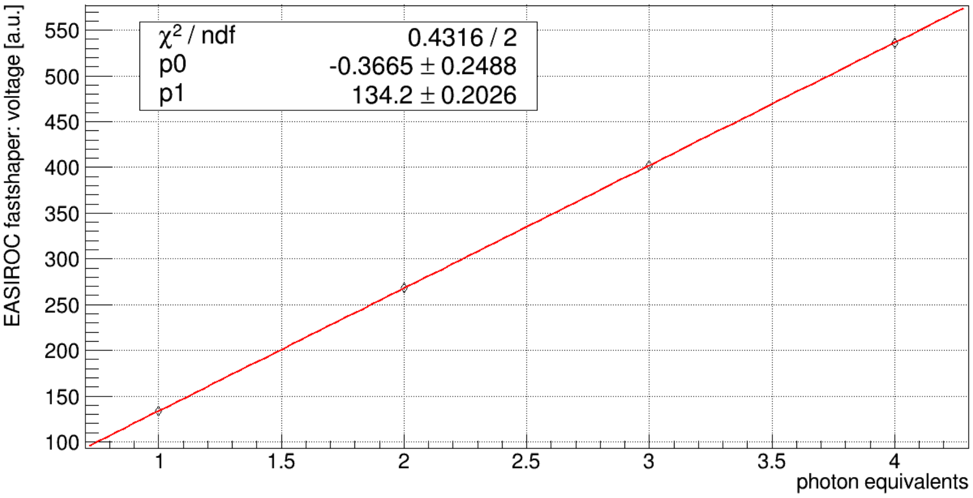

Figure 6.3: Calibration curve for the mapping between photo equivalents and the corresponding voltage from the shaped signal. As expected, the linear mapping fit to the data points as can be seen from the χ^2/ndf.

With the parameters of the linear regression $m = (132.9 \pm 0.4)\,\text{a.u.}\,\text{p.e.}^{-1}$ and $b = (1.0 \pm 0.6)\,\text{a.u.}$ the axis of the shaped voltage trace can be transformed into photo equivalents.

The sample contains 640000 noise simulations each over a $10\,\mu\text{s}$ time interval corresponding to a total simulated time of 6.4 s. A histogram of the maximal voltage values of the shaped signal from the EASIROC fast shaper within a time interval of $10\,\mu\text{s}$ can be seen in figure 6.4. The peaks correspond to the maximal voltages for the different photon equivalents. The bin value was increased by one entry for representation in the logarithm plot.

The number of noise simulation which exceed a voltage of 3 photon equivalents is rather small. In these simulations there were only 862 of 640000 events with 4 p.e. or higher (cf. figure 6.4). A histogram with a bin-width of 1 p.e. can be seen in figure 6.5. To estimate the maximal voltage value which can be exceeded by pure dark noise, a linear fit to the datapoints in figure 6.5 were done. The intersection of the line with the x-axis is interpreted as the maximal dark noise amplitude which occures for this sample size. This estimation provides a maximal threshold value of (5.93 ± 0.03) p.e. for these simulations (cf. figure 6.5).

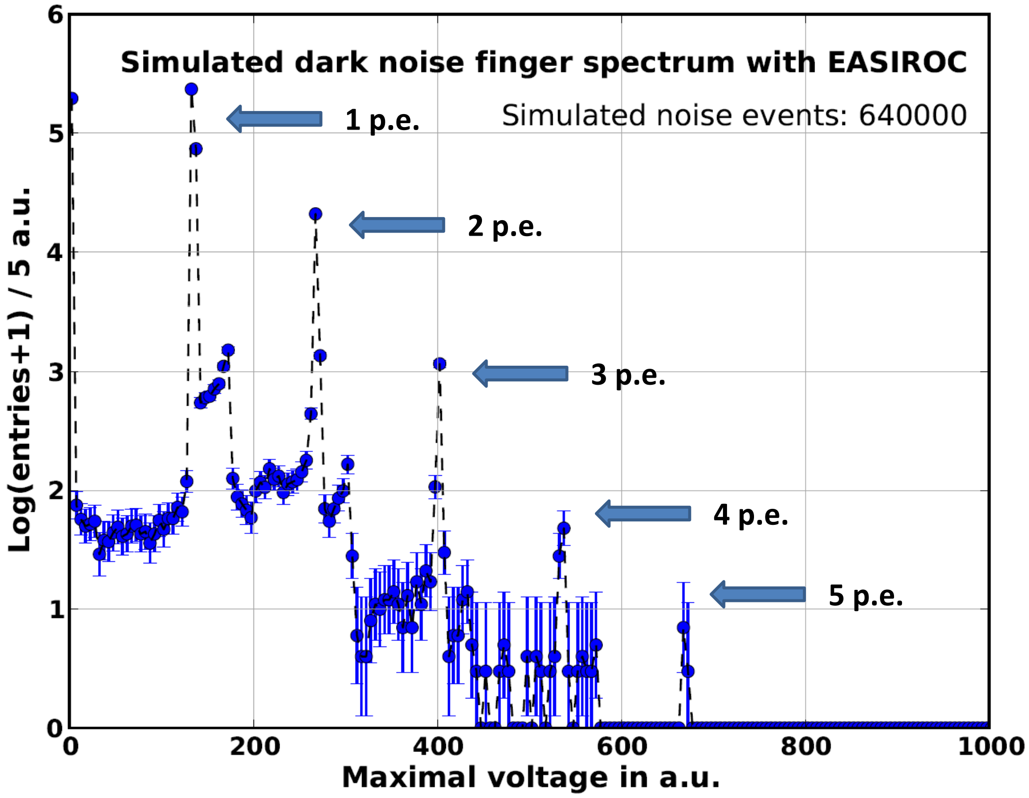

Figure 6.4: Decadic logarithm display of the histogram about the maximal voltage values of the EASIROC fast shaper signal within the time interval of $10\,\mu\text{s}$. The peaks correspond to the voltages for the different photon equivalents.

Since the statistic is limited to a samplesize of $N_{sample} = 640000$, the probability for a dark noise event which lead to more than 5.93 p.e. in a time interval of $10\,\mu$s is approximately

$$p = \frac{1}{640000} \approx 1.5 \cdot 10^{-6} \tag{6.3}$$

Thus, the probability to get a trigger by a dark noise event in the $10\,\mu$s time interval is negligibly small, assuming a simple trigger logic with a threshold value of 10 p.e.

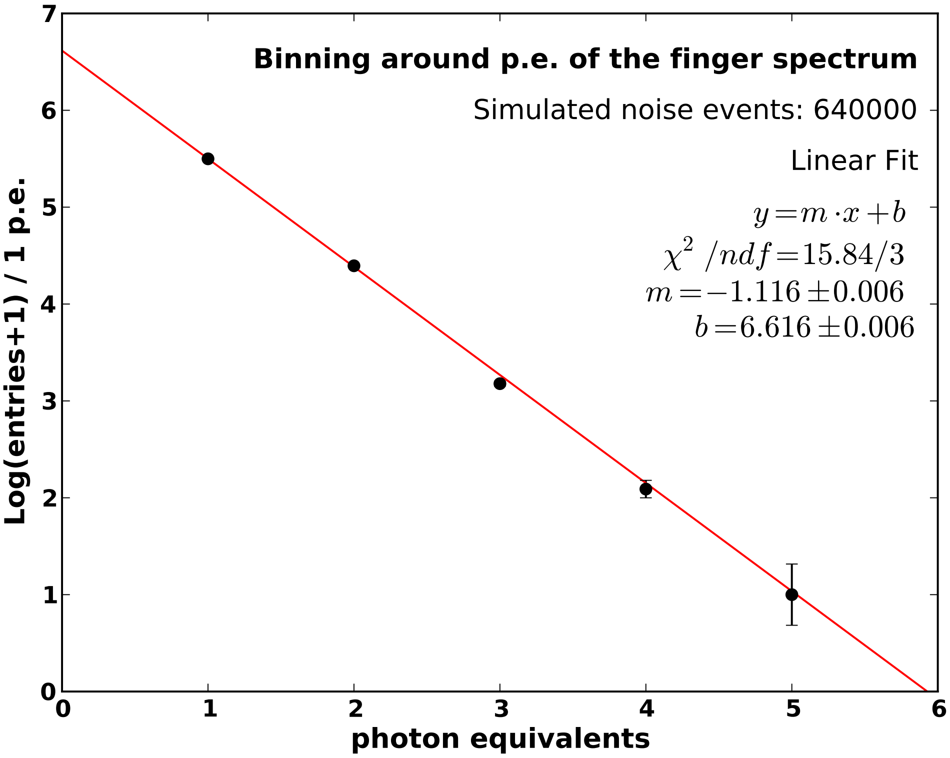

Figure 6.5: Decadic logarithm display of the histogram in 1 photon euivalent binning about the maximal voltage values of the EASIROC fast shaper signal with a time interval of $10\,\mu$s. A linear regression on the maxima provides an estimate for the maximal reached photon equivalents.

The dark noise rejection can be now determined as a function of the threshold value in photon equivalents. Thereby, threshold values of

$$n_{\text{thres}} = k + 0.5 \qquad k \in \mathbb{N}_0 \tag{6.4}$$

are investigated. The achieved dark noise rejection can be seen in figure 6.6. Already at a threshold of $n_{\text{thres}} = 3.5$ p.e. the dark noise rejection has increased almost to 100%. This means that there is almost not a single noise event, which leads to a false trigger. The number of photons, which hit the SiPM due to a traversing muon, is much higher (around $N_\gamma \approx 30$ simultaneously arriving photons) as will be shown in the further analysis. Therefore the high noise rate of SiPMs will not cause any problem in the case of AMD considering a time period of 10 μs.

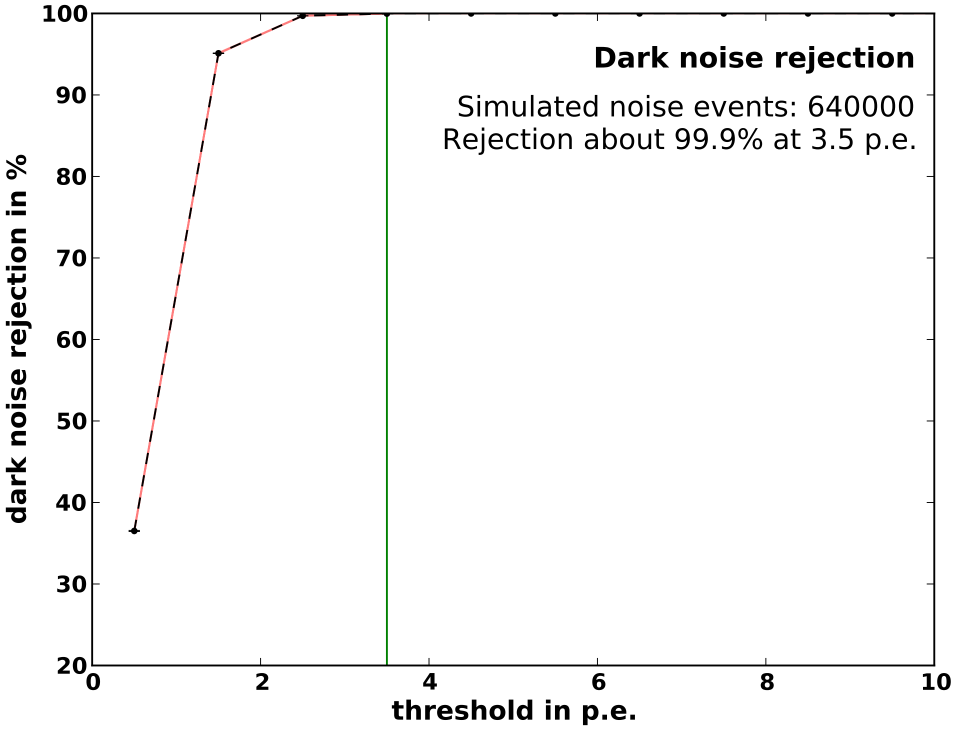

Figure 6.6: Dark noise rejection as a function of the threshold in photon equivalents. The rejection has already increased to over 99.9% at a threshold of 3.5 p.e..

6.2 Energy of muons in EAS from CORSIKA simulations

An essential part of this thesis is the determination of an optimised configuration regarding the geometry of the sigma fiber and the tile-size. This configuration is identified with single incoming particles which should have similar properties like the particles in a real EAS at the ground.

Therefore, this chapter provides an analysis of simulated showers from CORSIKA in order to adapt the simulated particles to the particles in a real extensive air shower (EAS). For this, 100 simulated EAS for a primary particle energy of 10^{18} eV, $10^{18.5}$ eV, 10^{19} eV, $10^{19.5}$ eV, 10^{20} eV and $10^{20.5}$ eV each with incidence angles of $\Theta = 0°, 20°, 40°$ and $60°$ respectively, were evaluated. Since many, especially low energy, particles get absorbed in the SD water tank before they can hit the AMD, these simulations already include the water tank.

Figure 6.7 shows an exemplary distribution of the energy for muons leaving the water tank. Due to the shielding of the tank, $\sim 99.3\%$ of the muons show energy levels of more than 10 MeV, since particles beyond an energy of the MIP energy strongly loose energy. The simulations include the hadronic interaction model. For all combinations of shower energy and incidence angle, the percentage of muons with an energy above 10 MeV is between 98% and 100%. For this purpose, the energy range between 10 MeV and 10^5 MeV for the simulated muons has been chosen.

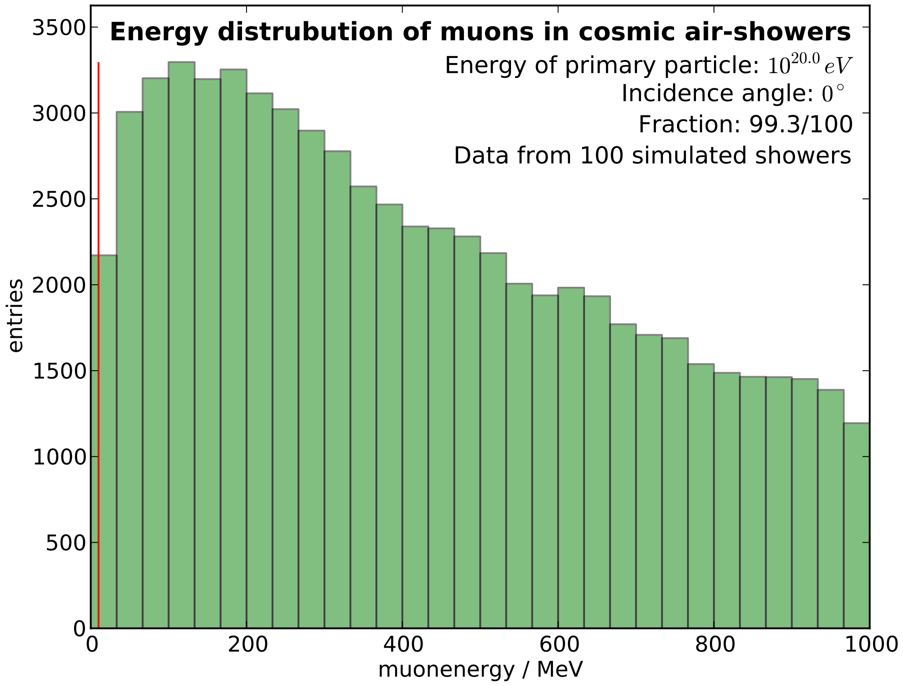

Figure 6.7: Energy distribution of muons of vertical EASs below the SD tank for a primary particle energy of 10^{20} eV. The red line marks an energy of 10 MeV. Approximately 99.3% of the muons have an energy above 10 MeV. 100 simulated air showers including the hadronic interaction model were used.

6.3 Photon yield

To optimise the efficiency for the trigger of muons, the trigger threshold U_{thres} has to be fixed first. This threshold should be as small, that the signal of nearly all traversing particles will be triggered. However, the threshold has to be at least $N_{\mathrm{thres}} = 3.5$ p.e. to reject the signal caused by dark noise. Therefore, in this section the expected number of photons by traversing particles is studied.

The photon yield N_γ is the number of simultaneous detected photons on the SiPM caused by a single traversing particle. As seen in figure 6.12, the distribution of the photon yield follows a Landau distribution, since the energy loss of charged particles while crossing matter following to the Bethe-Bloch formula. The most probable value (MPV) of this distribution can be considered as an indicator for the efficiency, since the efficiency includes the proportion of the

photon yield with values over the threshold value. However, the efficiency is also influenced by the width of the distribution.
The following results are based on several simulations. There is a set of 20000 muons and antimuons with energies between $10^{-1.5}$ MeV - $10^{5.75}$ MeV and incidence angles between 0° - 90° (cf. figure 6.8). A second set of 20000 muons and antimuons are simulated with energies between 10^{1} MeV - 10^{5} MeV and incidence angles between 0° - 10° (cf. figure 6.9). Moreover, there are sets of 20000 electrons and positrons with energies between 10^{-1} MeV - $10^{4.5}$ MeV (cf. figure 6.10) and 10000 protons with energies between 10^{-1} MeV - 10^{5} MeV (cf. figure 6.11), both with incidence angles between 0° - 90°. The simulations of the electrons and protons are done to estimate the signal which is caused by this undesired components of an EAS.
For nearly vertical muons, there are sets for each tile-size and each fiber configuration.

Figure 6.8 shows the distribution of the photon yield averaged over all incidence angles. Conspicuous is the significant deviation from the landau distribution for small numbers of produced photons. This effect results from very inclined muons, which interact with the steel support. In this case not the muon traverses a scintillating tile but several secondary particles. This can cause up to 10 simultaneous photon hits on the SiPM per secondary particle. This effect is significantly reduced as shown in figure 6.9, as the incoming muons have smaller incidence angles. Furthermore, the most probable value (MPV) decreases with lower incidence angle, due to the shorter path length which the muons travel in the scintillating tile. Since figure 6.8 contains an average over all incidence angles, the width of the distribution in 6.9 is also smaller.
As the incoming electrons, positrons and protons of the air shower are undesired, the triggered signals for these components should be as small as possible. Figure 6.10 shows the distribution of the photon yield for incoming electrons and positrons and in figure 6.11 for protons. Since the interactions with the steel support is more often for electrons, the peak at $N_\gamma < 10$ is much higher and should be cutted by the trigger. However, there remains an essential part of $\sim 3900/19702 \approx 20\%$ of the electrons which cause a number of photons larger than 10 p.e. (cf. 6.10). For the protons there is no visible Landau distribution any more, due to the strong absorbtion in the steel plate, leading to less protons reaching the scintillating tile. However, there is a small proportion of secondary particles which cause the peak at $N_\gamma < 10$. Using a threshold of $N_{thres} = 10.5$ p.e., the proportion of triggered protons is fortunately small $\sim 270/9938 \approx 2.7\%$.

In order to prevent a trigger caused by a secondary particle it is necessary to ensure that the threshold is at least $N_{thres} = 10.5$ p.e.. This affects the trigger efficiency of a real traversing muon only rarely, since the Landau distribution of muons is negligibly small in this region (cf. figures 6.9,6.15).

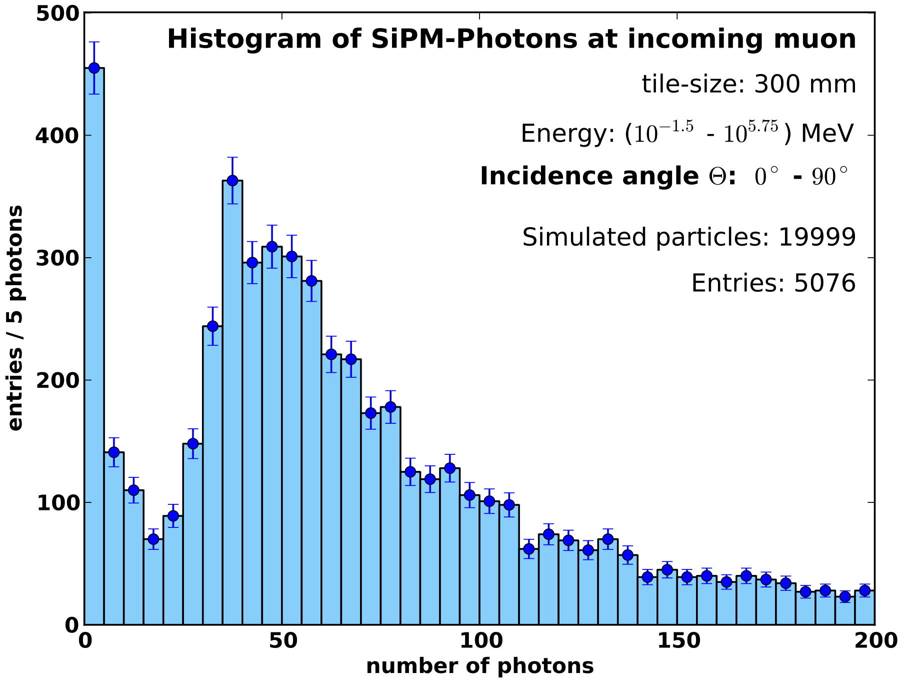

Figure 6.8: Histogram of photons detected by the SiPMs for a tile-size of $d = 300\,\mathrm{mm}$ and incoming muons and antimuons for all incidence angles.

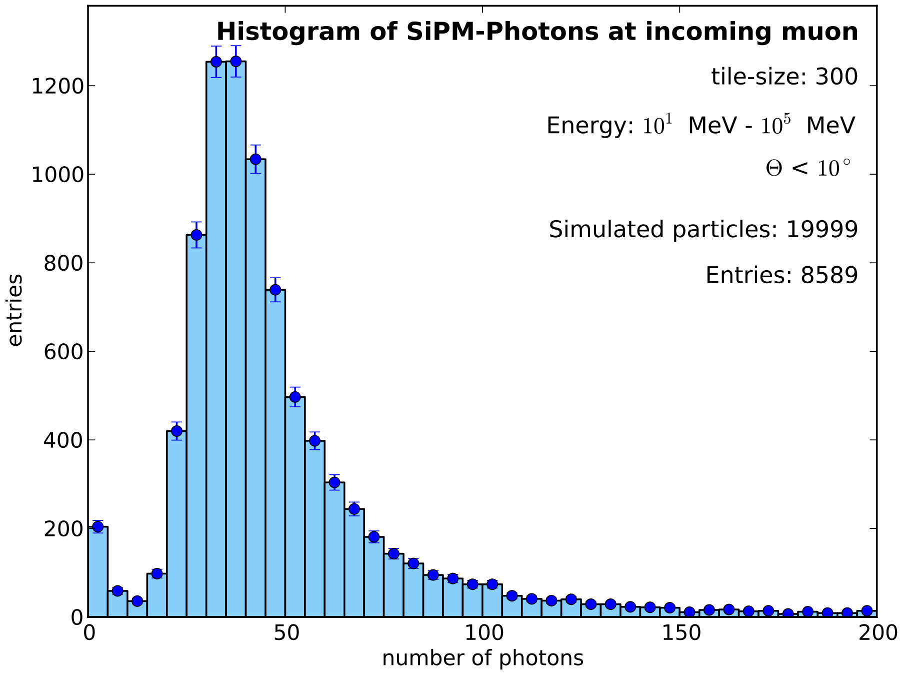

Figure 6.9: Histogram of photons detected by the SiPMs for a tile-size of $d = 300\,\mathrm{mm}$ and incoming muons and antimuons for incidence angles smaller than 10°.

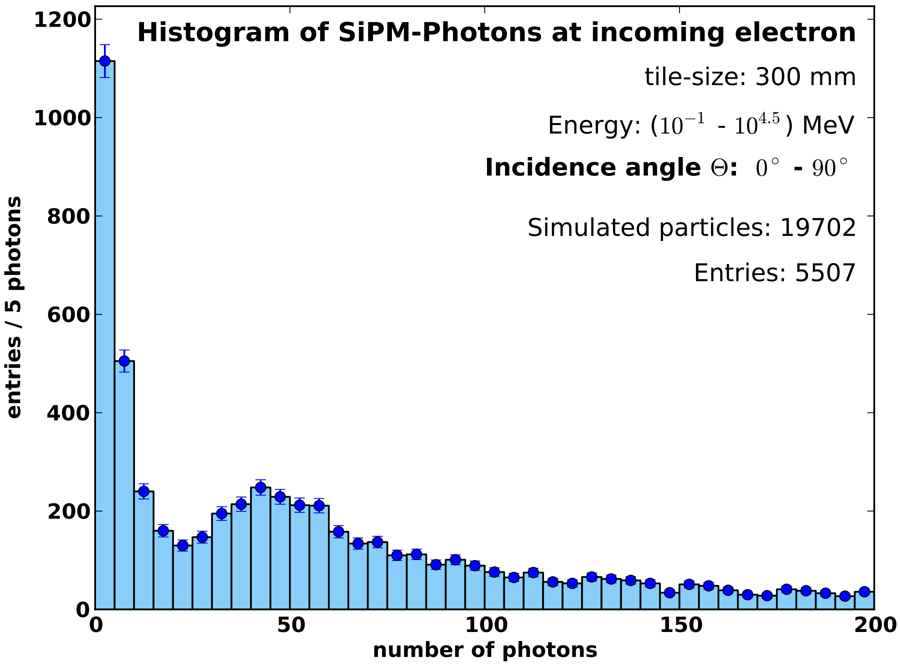

Figure 6.10: Histogram of photons detected by the SiPMs for a tile-size of $d = 300\,\mathrm{mm}$ and incoming electrons and positrons for all incidence angles.

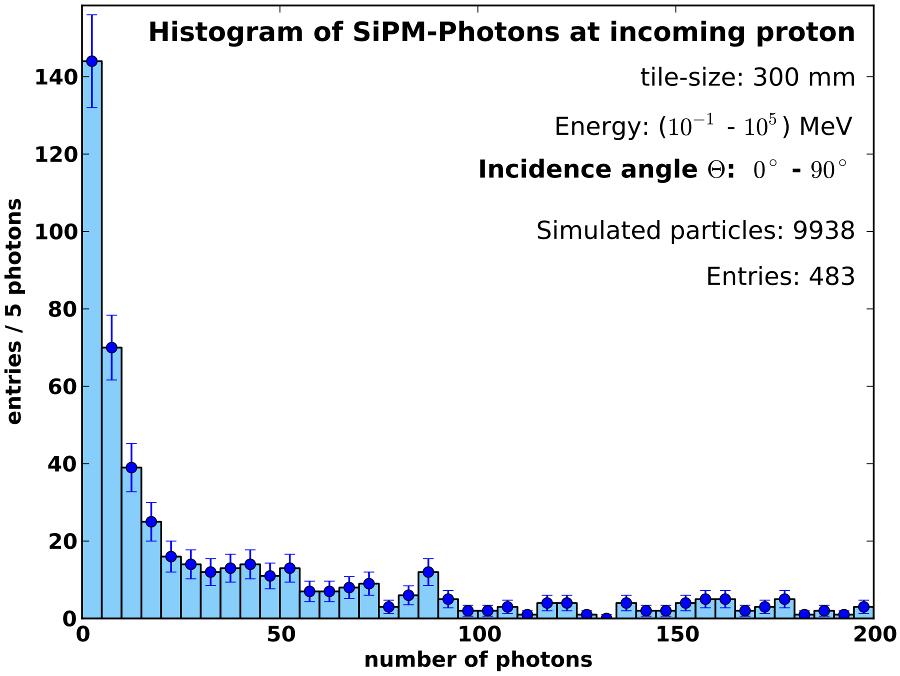

Figure 6.11: Histogram of photons detected by the SiPMs for a tile-size of $d = 300\,\mathrm{mm}$ and incoming protons for all incidence angles.

6.3.1 Landau fit

To calculate the MPV as an indicator for the trigger efficiency for a traversing particle a Landau distribution have to be fit to the photon yield (cf. Fig 6.12). Therefor, the sample of almost vertical (cf. figure 6.9) incoming muons, will be considered. For this case, the uncertainties of the MPV will decrease for the reason of a more distinct maximum. This is due to equal traveled distances in the scintillating tile as pointed out above.

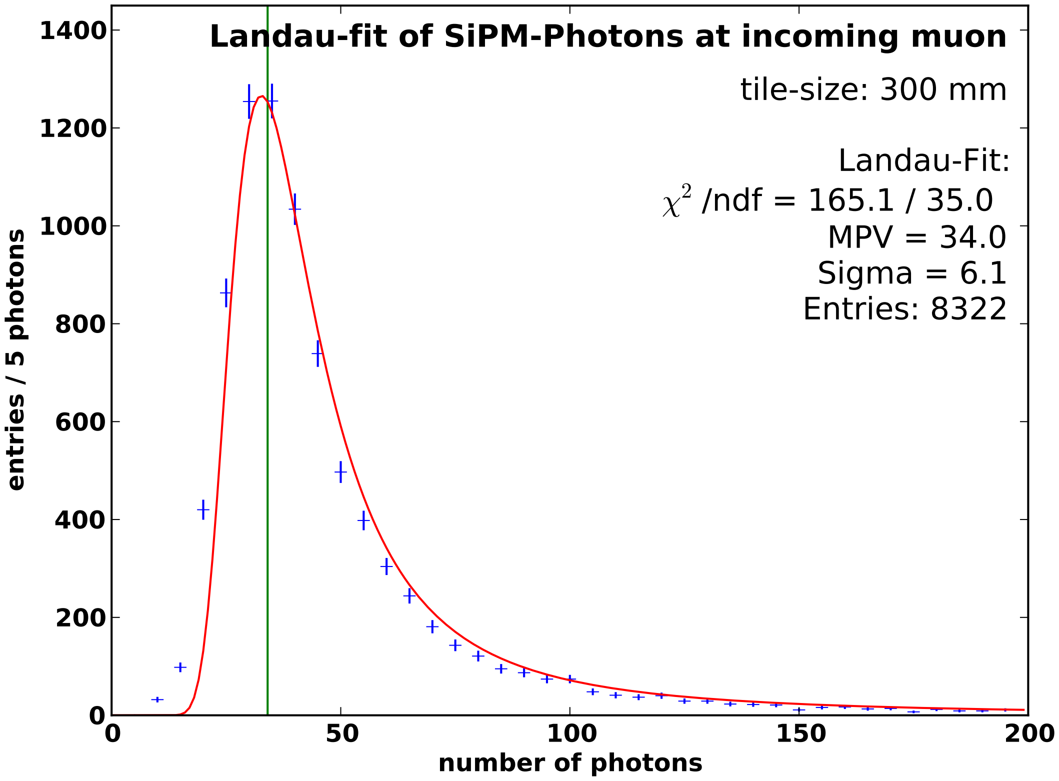

Figure 6.12: Landau fit to the distribution of photons detected by the SiPM after a muon crossed a scintillating tile. This distribution is shown in figure 6.9 except for the bins smaller than 10 p.e.. The relatively high χ^2/ndf represents the fact that the distribution is not described by a pure Landau distribution, since there are Gaussian processes regarding the production of photons and the transmission into the WLS fiber.

Since the peak for $N_\gamma < 10$ contains mostly events of secondary particles and not the number of emitted photons, while the crossing of a muon, the fit does not consider values for $N_\gamma < 10$. As can be seen in figure 6.12, the model of a pure Landau distribution does not optimally fit the data points. This is also represented by a high χ^2/ndf. The landau distribution describes the energy deposition in the scintillating tile, which is not identical with the photons reaching the SiPM, since the transformation of the energy into photons, the transmission of the photons into the sigma fiber and the photon losses in the waveguide also play an important role. However, the fit of a landau distribution convolved with a Gaussian distribution would not improve the situation, since there are too many unknown components.

Another reason for the systematically too high χ^2/ndf is that the distribution in figure 6.9 is an average over many different tile positions. The next chapter shows the Landau fit seperated by different length of waveguides.

6.3.2 Dependence on the length of the waveguide

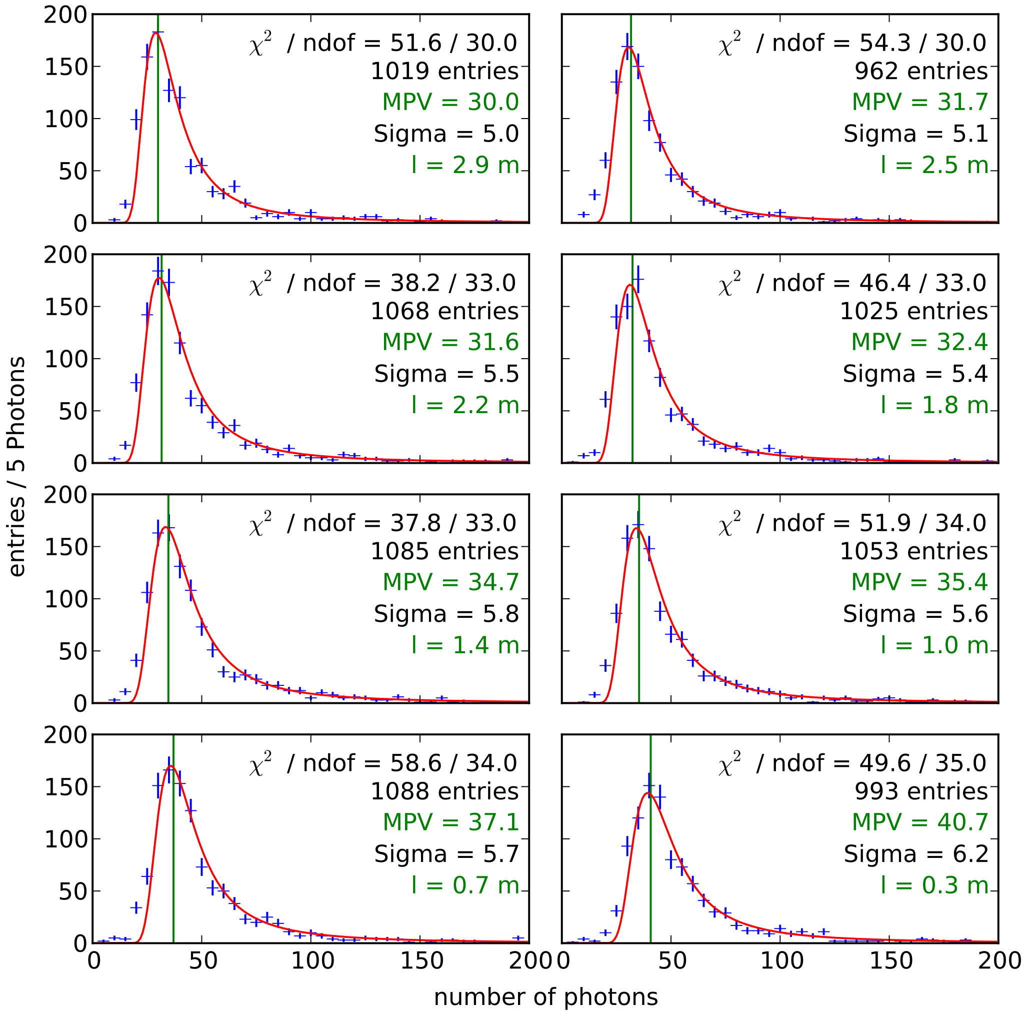

Figure 6.13: Landau fit for different tile positions and therefore different waveguide length for muons with incidence angles below 20°. The MPV shows a clear dependence on the waveguide length l due to the higher photon loss rate, during the transport.

The scintillating tiles have different distances to the SiPMs depending on their positions. A higher distance means a longer waveguide and therefore a higher probability for photon losses in the waveguide. This will influence the MPV of the Landau distribution as can be seen in figure 6.13.
Whereas the MPV for a waveguide length of $l = 0.3\,\mathrm{m}$ is still 40.7 p.e., the MPV drops to 30 p.e. at a length of $l = 2.6\,\mathrm{m}$. This effect could affect the trigger efficiency of a tile on the far side of the SiPM in comparison to a tile next to the SiPM, for the case of a small mean MPV.
On average the MPV of the Landau fit to the combined distribution (cf. figure 6.12) represents the performance of the different configurations very well, since this thesis should figure out an optimised configuration for the whole AMD. Therefore, the subsequent definition of the MPV refers to the fit of the combined distributions. This value is very close to the mean of all MPVs of the different wavelength in figure 6.13.

6.4 Optimal threshold for the triggering of muons

To calculate the efficiency for detecting single incoming muons, an optimal threshold value has to be determined. Analogously to the approach to calculate the dark noise rejection, this section will show the trigger efficiency as a function of the threshold value in photon equivalents. Therefor, the set of vertical incoming muons with an incidence angle below 10° is used.

Figure 6.14 shows the chronological signal by photon hits and noise phenomena with a binning of 100 ns. The peak at $t \approx 0\,\mathrm{ns}$ results from the photons, which are produced through the traversing muon and correlated noise. There are two additional signals which are comparatively small and caused by thermal noise. To calculate the efficiency as a function of the threshold, the efficiency is scanned in the same threshold steps like the dark noise rejection:

$$n_{thres} = k + 0.5 \qquad k \in \mathbb{N}_0 \quad . \tag{6.5}$$

The trigger efficiency as shown in figure 6.15 is the share of events, where the shaped voltage trace is higher than the threshold value in all events. An optimal threshold value would be characterised by an exeeding from all voltage traces of muon signals but at once the threshold value should not be gained by any dark noise event.

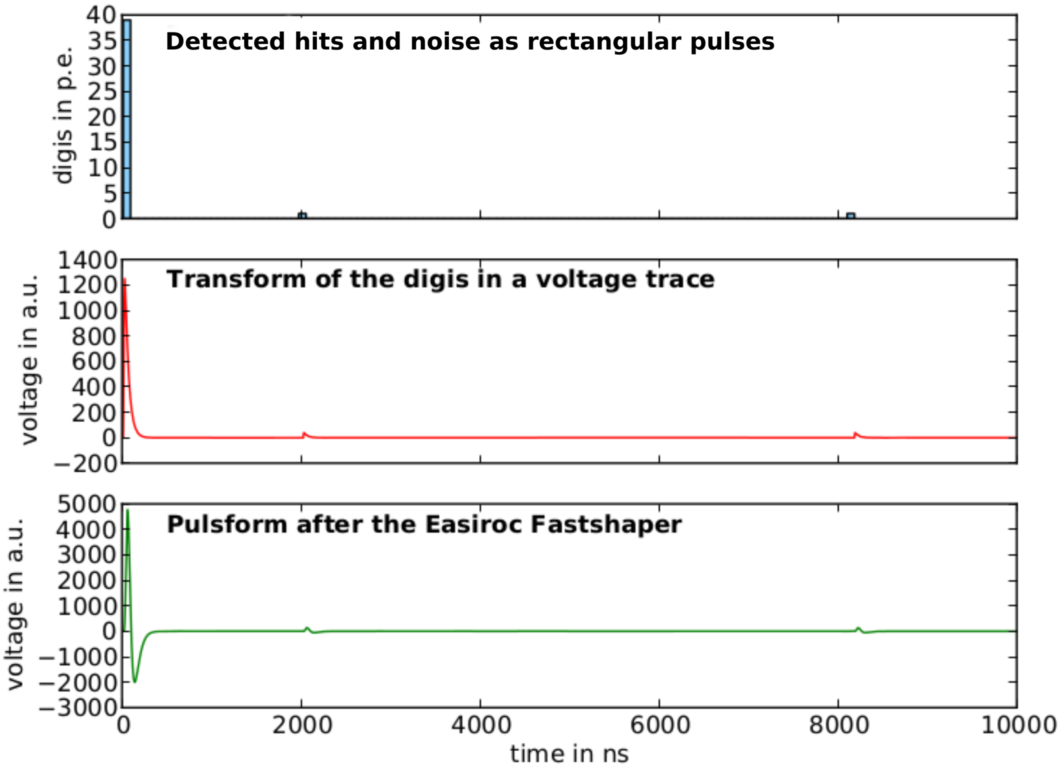

Figure 6.14: Simulated muon events including noise of the Hamamatsu silicon photomultiplier. The digis show the chronological signal of cell breakdowns by hits and noise phenomena. The middle figure is the resulting voltage trace and the figure on the bottom the signal from the EASIROC fastshaper.

To determine the optimal threshold value, one could imagine to take the intersection of this curve and the dark noise rejection. For this case, both the trigger efficiency and the dark noise rejection are fortunately high, about 99.5%. However, this would lead to a threshold from 2.5 p.e. and in turn lead to many trigger events, caused by secondary particles. For this reason, the threshold should be at least $N_{thres} = 10.5$ p.e. as discussed in chapter 6.3. The trigger efficiency would be still sufficient high, 98.7% for the tile-size of 300 mm.

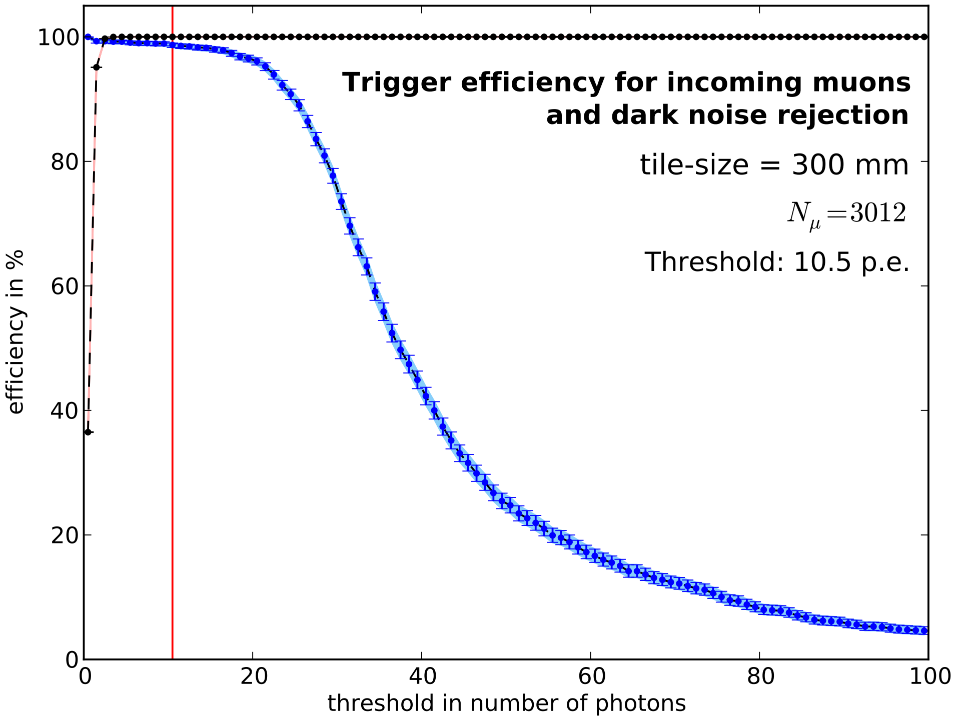

Figure 6.15: Trigger efficiency (blue) and dark noise rejection (red) as a function of the trigger threshold for a tile-size of $d = 300$ mm. The optimal threshold should have a dark noise rejection about 99.99%, but at least 10.5 p.e.. At the same time the trigger efficiency should not have dropped below 95%.

6.5 Trigger efficiency

This section accurately define how the efficiency will be calculated for the following optimisation studies. This work distinguishes between two effiencies, the efficiency of a single tile on the one hand and the efficiency of the complete AMD on the other hand. The particles are simulated uniformally distributed in the x-y plane on the upper side of the steel support plate.

The selection of the simulated muons, which are taken for the determination of the **efficiency of a single tile** ϵ_{tile} is presented in figure 6.16. Only the muons which can hit a scintillating tile for geometrical reasons are considered, leading to the number of muons N_{tile}. The muons are generated at a distance $d = 72.6$ mm above the scintillating tiles according to the position of the steel support plate (cf. 6.16). Therefore, a muon with incidence angle θ can travel a distance $r = d \cdot \tan(\theta)$ in the x-y-plane. If the x- or y-coordinate of the start point of a muon differs more than $d_{\text{pitch}}/2 - r$ from the closest center of a scintillating tile, the muon is not accepted (cf. figure 6.16). The efficiency of a single tile is therefore defined as:

$$\epsilon_{\text{tile}} == \frac{N(N_\gamma > N_{\text{thres}})}{N_{\text{tile}}} \leq 1 \quad . \tag{6.6}$$

$N(N_\gamma > N_{\text{thres}})$ represents the part of events, where at least $N_{\text{thres}} = 10.5$ photons are registered on any SiPM.

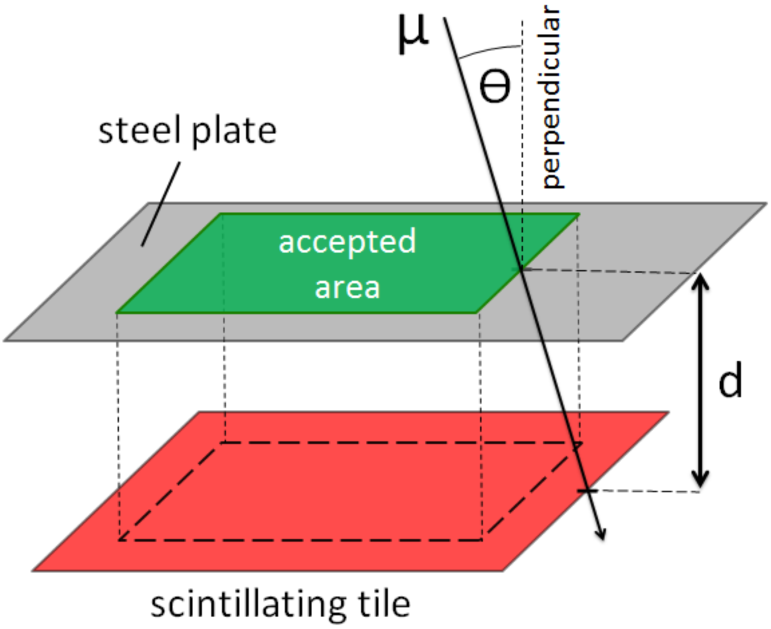

Figure 6.16: Sketch of the geometrical selection of the muons for calculating the efficiency of a single tile. Only muons, which can hit the scintillating tile for geometrical reasons, will be considered for the calculation. The muons can travel the distance $r = d \cdot \tan(\theta)$ on the tile plane according to the incidence angle θ. d is the vertical distance between the tile and the steel plate.

In contrast, for the **efficiency of complete AMD** ϵ_{AMD} all muons which "start" within the profile of the whole steel support construction in the height d above the scintillating tiles are considered. This total number N_{AMD} also includes muons, which cannot hit the AMD for geometrical reasons. The numerater in the efficiency ϵ_{AMD} (cf. equation (6.7)) is calculated through the fraction of events in N_{AMD}, where at least $N_{\text{thres}} = 10.5$ photons are registered on any SiPM:

$$\epsilon_{\text{AMD}} = \frac{N(N_\gamma > N_{\text{thres}})}{N_{\text{tile}}} \leq 1 \quad . \tag{6.7}$$

In the following a threshold value $N_{thres} = 10.5$ will be used according to the determined optimal threshold value for the trigger efficiency of AMD for single muons.

6.6 Finding an optimised tile-size

To find an ideal size for the scintillating tile, simulations with tile-sizes of 260 mm, 280 mm, 300 mm, 320 mm, 340 mm and 360 mm will be analysed.

Since the efficiency for the trigger of a muon is only influenced by the simultaneous number of photons which reach the SiPM in this simple model of a trigger, the MPV as a benchmark for the photon yield for different tile-sizes will be considered first. The fit of Landau distributions to the distribution of incoming photons on the SiPM for these simulations show a clear correlation between the MPV and the tile-size (cf. figure 6.17).

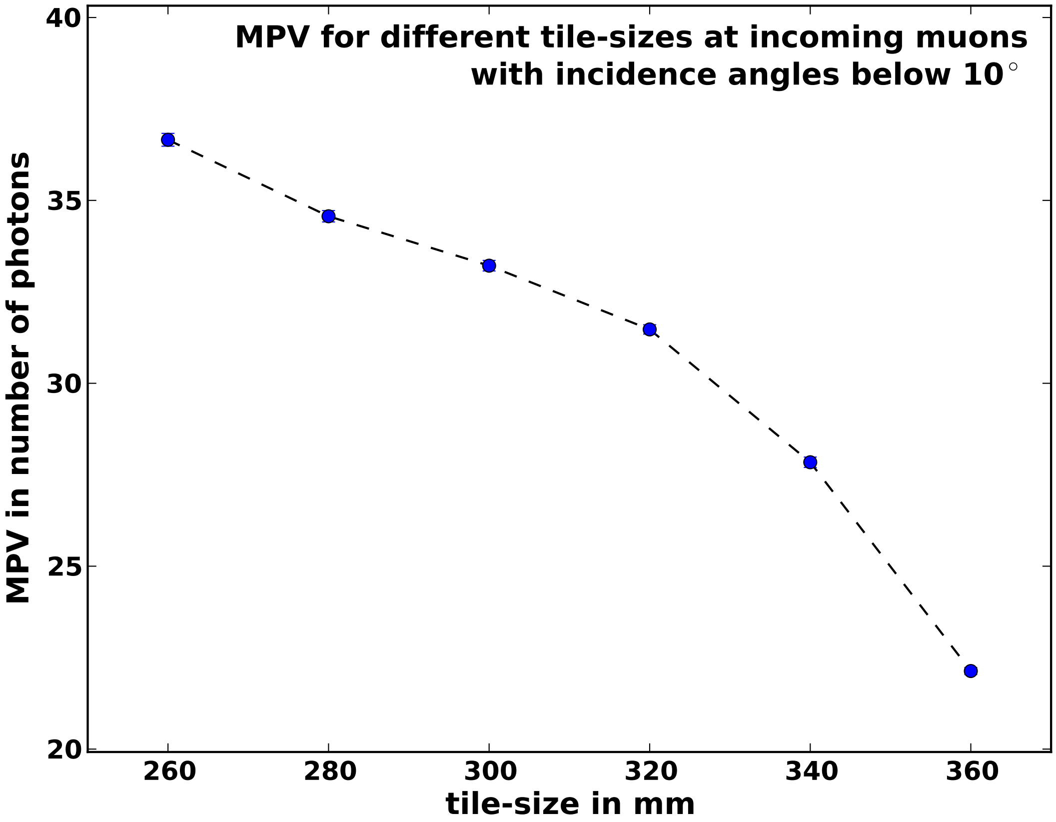

Figure 6.17: MPVs from Landau fits for simulations with incoming muons with incidence angles below 10° and different tile-sizes between 260 mm and 360 mm. The MPV shows a clear dependence on the tile-sizes, since the photon loss in the tiles increase with a higher distance to the sigma fiber.

The MPV and therefore the photon hits on the SiPM decreas with increasing tile-size. This is due to a higher photon loss probability in the scintillating tile. This is caused by an increasing number of reflections on the boundaries, since the mean distance between the photon production point and the sigma fiber increases (cf. figure 5.6) as the fiber-padding and the fiber-radius are kept fixed.

To get a higher photon yield in the single tiles, the tile-size has to be as small as possible. However, this will reduce the fill factor α_{d} of the sensitive area

$$\alpha_d = \frac{64 \cdot d^2_{\mathrm{tile}}}{A_{\mathrm{AMD}}} \tag{6.8}$$

and therefore the efficiency of the complete AMD ϵ_{AMD} (cf. figures 6.18,6.19) with the total cross-section area A_{AMD} of the whole AMD. Hence, one has to find a compromise between these effects.
Considering the efficiency of a single tile ϵ_{tile} in figure 6.18 and 6.19 one can see that the decreasing MPV has a first effect on the efficiency above a tile-size of $d = 320\,\mathrm{mm}$.

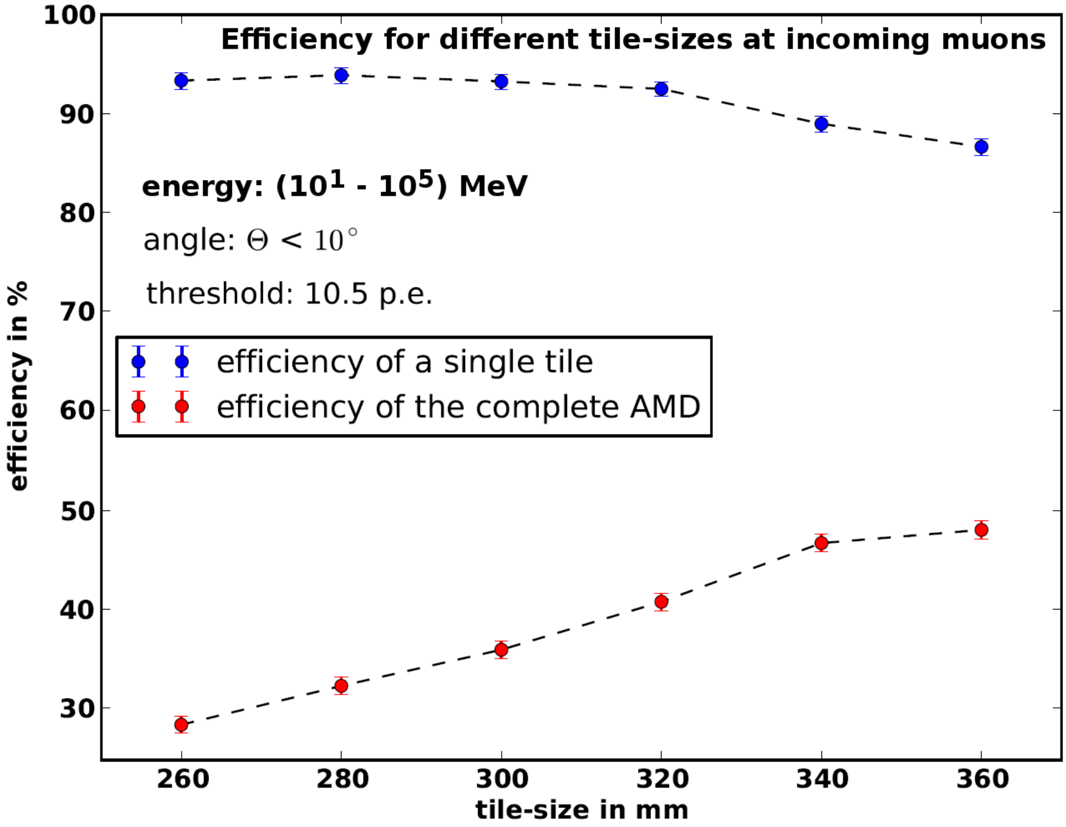

Figure 6.18: The efficiency ϵ_{tile} for a single tile and the efficiency ϵ_{AMD} for the complete AMD for different tile-sizes. The simulated muons have incidence angles below 10° and an energy range between 10 MeV and $10^{5.75}$ MeV.

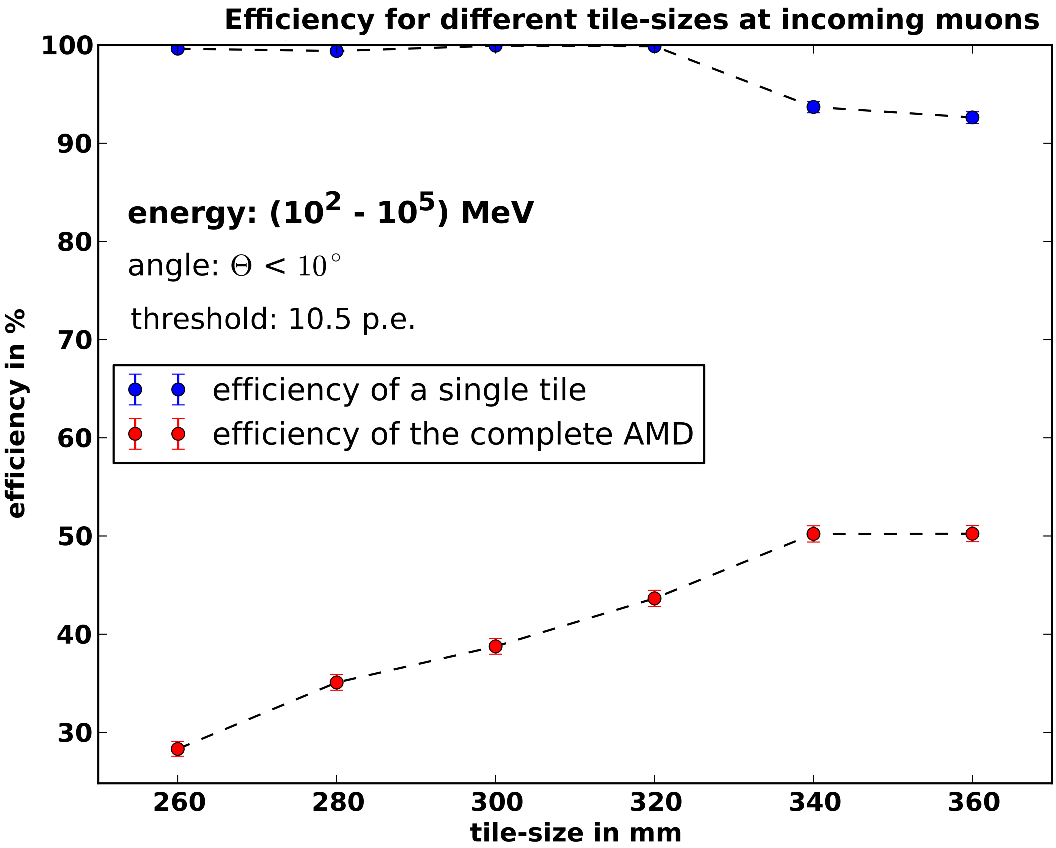

Figure 6.19: The efficiency ϵ_{tile} for a single tile and the efficiency ϵ_{AMD} for the complete AMD for different tile-sizes. The simulated muons have incidence angles below 10° and an energy range between 10^2 MeV and $10^{5.75}$ MeV.

For this reason, a tile-size of $d = 320\,\text{mm}$ would be an ideal size to find a compromise between the photon yield and therefore the efficiency for a single tile ϵ_{tile} on the one hand and the geometrical fill factor and therefore the efficiency of the complete AMD ϵ_{AMD} on the other hand. This tile-size is therefore also used for all further simulations.

The efficiency for triggering a vertical single muon with an energy between 10 MeV and 10^5 MeV is approx 92% for a tile-size of $d = 320\,\text{mm}$ (cf. figure 6.18). Considering the same muons with energies about 100 MeV leads to an efficiency of almost 100% (cf. figure 6.19), since the muon does not interact in the steel support any more.

6.7 Finding an optimised fiber configuration

To find an optimised configuration for the two parameters fiber-padding and fiber-radius (cf. figure 5.3), a sample of 10000 muons for a tile-size of 320 mm is used. The muons have incidence angles smaller than 10° and an energy between 10 MeV and 10^5 MeV for each configuration. As previous simulations have shown, the fiber-padding should be very small in the dimension of 10 mm, due to a higher possibility for the photons to enter the sigma fiber. For the padding the values $p = 2.5\,\mathrm{mm}$, $p = 5\,\mathrm{mm}$, $p = 7.5\,\mathrm{mm}$, $p = 10\,\mathrm{mm}$, $p = 12.5\,\mathrm{mm}$ and $p = 15\,\mathrm{mm}$ were simulated and for the radius $r = 50\,\mathrm{mm}$, $r = 55\,\mathrm{mm}$, $r = 60\,\mathrm{mm}$, $r = 65\,\mathrm{mm}$, $r = 70\,\mathrm{mm}$ and $r = 75\,\mathrm{mm}$. Therefore, there are 36 different configurations and a sample of 360000 simulated muons.

Due to the high sample size, the uncertainties of the MPV is rather small. Thus, the deviation between the highest and the lowest MPV is larger than eight standard deviations. This allows a discrimination between different configurations regarding the shape of the sigma fiber.
The simulations show a preference for small paddings regarding the MPV. However, the padding should be at least $p = 5\,\mathrm{mm}$, since the MPV is significantly smaller for a padding below $p = 5\,\mathrm{mm}$. The region with a configuration between $p = 5\,\mathrm{mm}$ - $p = 10\,\mathrm{mm}$ and $r = 55\,\mathrm{mm}$ - $r = 75\,\mathrm{mm}$ shows a good performance, whereby the evident maximum within this area is at the configuration with a padding of $p = 5\,\mathrm{mm}$ and a radius of $r = 55\,\mathrm{mm}$.

The previous analysis figured out an **optimised geometrical configuration** regarding the tile-size d, the fiber-padding p and the fiber-radius r with the values:

$$d = 320\,\mathrm{mm} \qquad p = 5\,\mathrm{mm} \qquad r = 55\,\mathrm{mm}$$

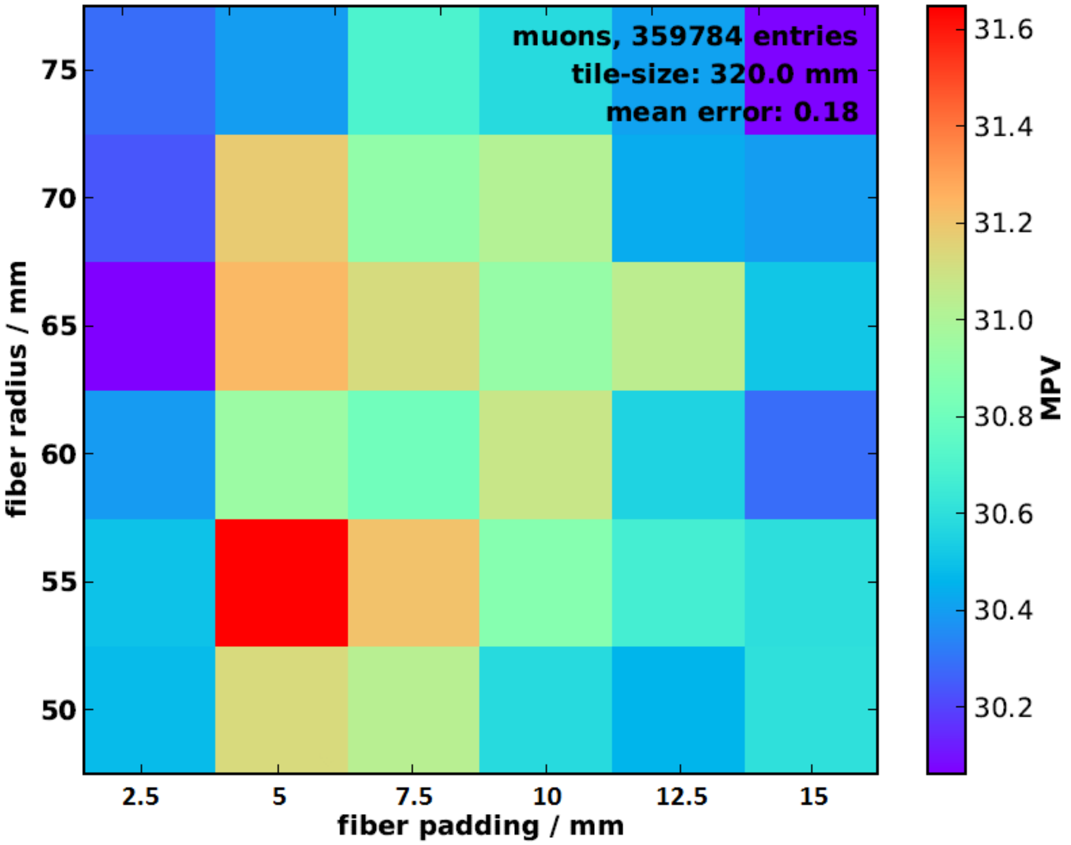

Figure 6.20: MPVs from landau fits for simulations with incoming muons with incidence angles below 10° and different fiber configurations with paddings between $p = 2,5\,\mathrm{mm} - 15\,\mathrm{mm}$ and radii between $r = 50\,\mathrm{mm} - 75\,\mathrm{mm}$.

6.8 Comparison between multiclad and singleclad fiber

This chapter contains a comparison of the multiclad fiber and the singleclad fiber for the use as sigma fiber and waveguide in the setup of AMD. The simulation sample includes 100000 muons with incidence angles smaller than 10° and energies between 10 MeV and 10^5 MeV both for the multiclad fiber and the singleclad fiber.

Figure 6.21 shows the MPV seperated for different fiberlength of the multiclad and the singleclad fiber. For all tile-position the MPV of the multiclad fiber is between 5 and 8 photon equivalents higher than the MPV of the singleclad fiber. This means that there are more photons which reach the SiPM for the multiclad fiber and in turn an improved efficiency. The results of these simulations do not correspond with the expectation that the transmission of the photons into the fiber is worse in case of the multiclad fiber, due to the smaller refractive index of the outer cladding. However, the more efficient photon confinement while the transport within the curved sigma fiber could be an explanation for this effect.

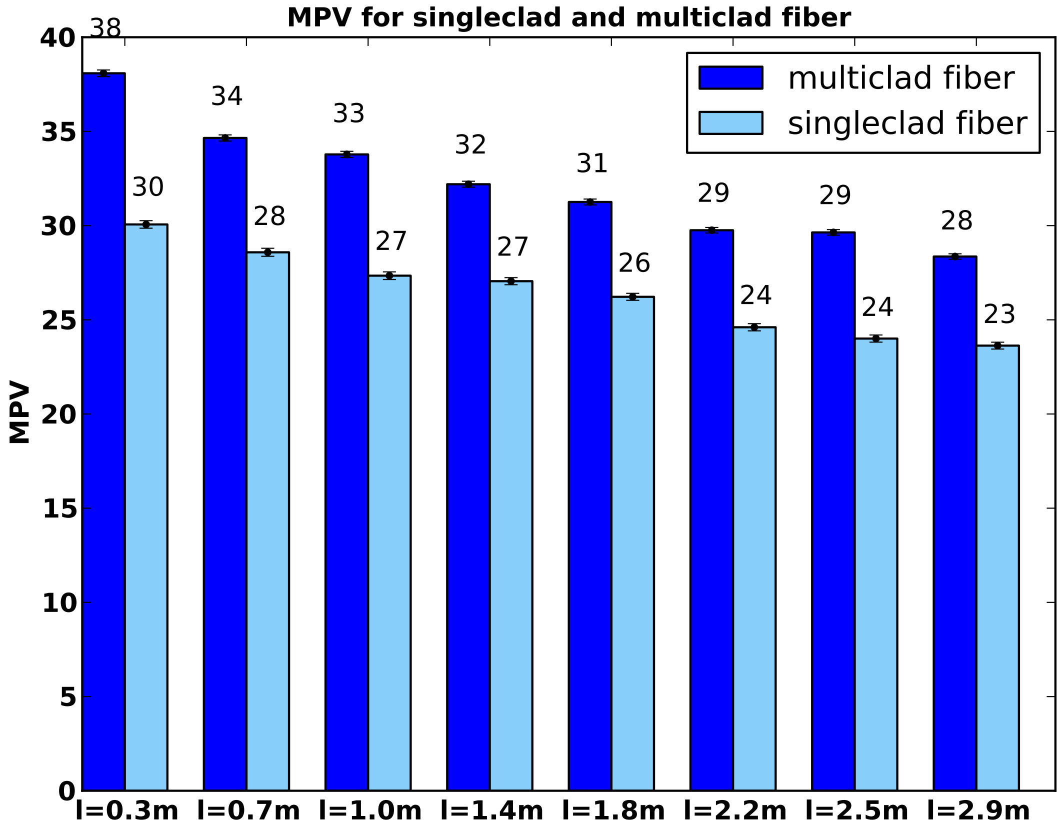

Figure 6.21: MPVs from Landau fits for the singleclad and the multiclad fiber seperated for different fiberlength (cf. figure 6.13). The optimised geometrical configuration of AMD (tile-size $d = 320\,\text{mm}$, fiber-padding p and fiber-radius r) is used.

In a second step the uniformity of the photon hits on the SiPM is studied. A more uniform illumination of the SiPM surface also means a more equal demand of each photodiode and therefore a higher dynamic range.

The performance of the multiclad fiber regarding the uniformity of photon hits on the SiPM surface is better as well. This distribution is much more uniform for the multiclad fiber than the distribution of the singleclad fiber (cf. figures 6.22 and 6.23). As can clearly be seen in figures 6.22 and 6.23, most photon hits are within a circle with diameter 1 mm. In the corner regions there are considerably less photon hits anymore. This is due to the circular cross-section area of the waveguides which ends onto the surface of the SiPMs. The uniform the distribution on the SiPM surface, the more equal the stress for each photodiode. This also means a higher dynamic range for the SiPM.

For this reasons, the multiclad fiber is more adequate for the use as sigma fiber and waveguide in the setup of AMD.

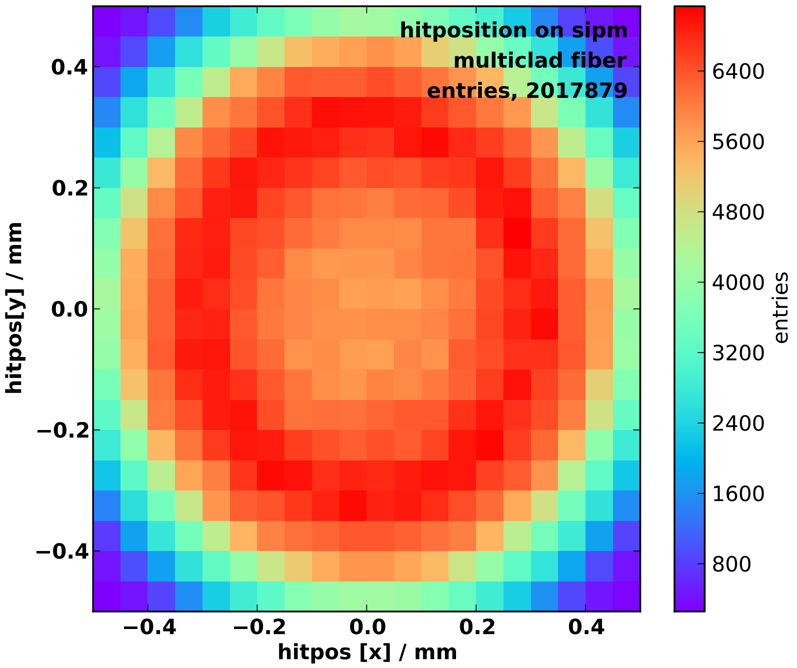

Figure 6.22: Photon hit distribution on the 1 mm^2 surface of the SiPM for incoming muons. The optimised configuration and the multiclad model for the optical fibers have been used.

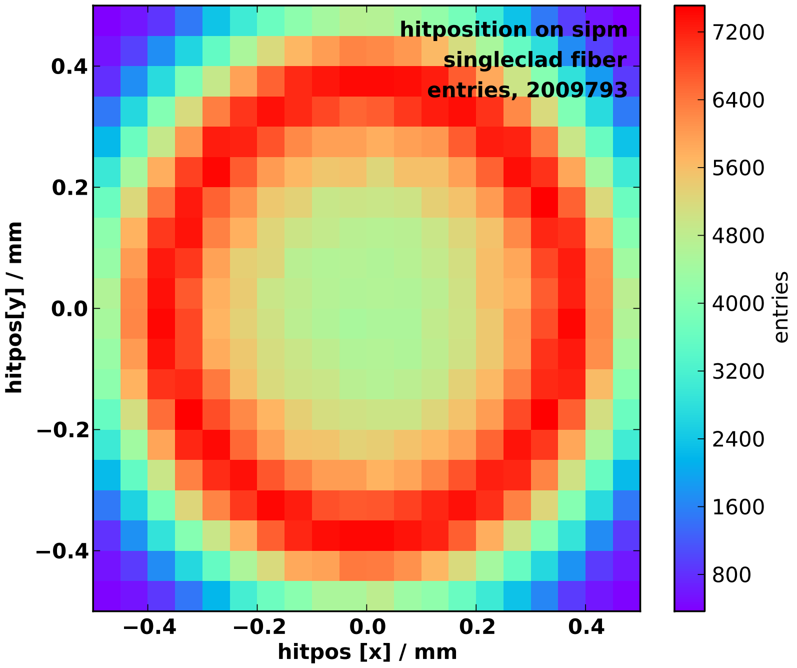

Figure 6.23: Photon hit distribution on the 1 mm^2 surface of the SiPM for incoming muons. The optimised configuration and the singleclad model for the optical fibers have been used.

7 Conclusion

The Aachen Muon Detector (AMD) is a proposal for the Pierre Auger update program 2015 for the measurement of the muonic component of extensive air showers. A prototype is designed and built by our working group at the III. Physikalisches Institut A, RWTH Aachen. The basic concept is the detection of muons by a combination of scintillating tiles, in which light is produced by traversing charged particles, and optical fibers for the transport of the produced photons to the light sensor, an SiPM. This thesis outlined several performance studies to determine the optimal geometry and setup for the detector.

The distribution of detected photons on the SiPM follows a Landau distribution. The most probable value (MPV) of this distribution for traversing muons is a good benchmark for the efficiency of the detector. Simulations with different values for the parameters tile-size d, fiber-radius r and fiber-padding p in the setup of AMD were analysed. The optimised configuration regarding this parameters for the trigger efficiency of single muons is:

$$d = 320\,\mathrm{mm} \qquad p = 5\,\mathrm{mm} \qquad r = 55\,\mathrm{mm}$$

The influence of the dark noise of the SiPMs on the signal caused by a traversing muon has been investigated and is negligible. The possibility for a noise event with more than 3 photon equivalents in a time interval of 10 μs, which is a typical time period of an incoming extensive air shower is approximately 0.2%. In contrast, the signal of a muon crossing is approximate 40 photon equivalents. Therefore, the noise phenomena have practically no influence on the trigger of muons for an adequate threshold value of 10.5 photon equivalents. This threshold has to be chosen to prevent triggers which are caused by the production of secondary particles, as found out during the simulation studies.

For the BCF-92 WLS sigma fiber and the BCF-98 waveguide in the setup of AMD, simulations were done both for the singleclad fiber and the multiclad fiber. The photon yield of the SiPM for the multiclad fiber is about 5 photon equivalents higher than the photon yield for the singleclad fiber. In addition, the distribution of SiPM photon hits is more uniform for the multiclad fiber, raising the dynamic range for the AMD in comparison to the singleclad fiber. For this reason, the multiclad fiber should be used as optical fibers to improve the performance of AMD.

This simulation study optimised the geometry for the AMD regarding the performance for the trigger of muons. The promising prototype is suited for a successful measurement of the muonic component of cosmic rays air showers.

References

[1] G. Federmann. ”Victor Hess und die Entdeckung der Kosmischen Strahlung”. Diplomarbeit, Universität Wien, 2003.

[2] M. Bustamante et al. ”Origin of cosmic rays”. 2012.

[3] D. Meschede. *Gerthsen Physik.* Springer, Berlin, 2010.

[4] L. Drury. ”High-energy cosmic-ray acceleration”. 2009.

[5] Pierre Auger Collabaration. ”Muons in air showers at the Pierre Auger Observatory: Measurement of amospheric production depth”. 2014. arXiv:1407.5919v1.

[6] Particle Data Group. ”Cosmic rays”. 2013.

[7] M. Domenico et al. ”Reinterpreting the development of extensive air showers initiated by nuclei and photons”. 2013. arXiv:1305.2331v2.

[8] Particle Data Group. *Particle Physics Booklet.* California, 2010.

[9] W. Demtröder. *Experimentalphysik 4. Kern-, Teilchen und Astrophsik.* Springer, California, 2010.

[10] H. Dembinski. ”Aufbau einer Detektorstation aus Szintillatoren zum Nachweis von kosmischen Teilchenschauern, Simulation und Messung”. Diplomarbeit, RWTH Aachen University, 2005.

[11] M. Lemoine. *Physics and Astrophysics of Ultra-High-Energy Cosmic Rays.* Springer, Berlin, 2001.

[12] Pierre Auger Collabaration. Taken from: http://www.scinexx.de/dossier-bild-353-6-8969.html (Access: 7.9.2014 10:14 AM).

[13] S. Fliescher. ”Radio Detection and Detector Simulation for Extensive Air Showers at the Pierre Auger Observatory”. Diplomarbeit, RWTH Aachen University, 2005.

[14] C. Peters. ”Design Studies for an Air Fluorescence Telescope with Silicon Photomultipliers for the detection of Ultra high energy Cosmic Rays”. Masterarbeit, RWTH Aachen University, 2013.

[15] T. Niggemann. ”New Telescope Design with Silicon Photomultipliers for Fluorescence Light Detection of Extensive Air Showers”. Masterarbeit, RWTH Aachen University, 2012.

[16] Pierre Auger Collabaration. ”The Fluorescence Detector of the Pierre Auger Observatory”. 2009. arXiv:0907.4282.

[17] M. Grigat. ”Large Scale Anisotropy Studies of Ultra High Energy Cosmic Rays Using Data Taken with the Surface Detector of the Pierre Auger Observatory”. Doktorarbeit, RWTH Aachen University, 2011.

[18] Pierre Auger Collabaration. ”The Next Frontier in UHECR Research with an Upgraded Pierre Auger Observatory”. 2013. arXiv:1307.0226v3.

[19] FZU IFSC/USP LIP et al, CBPF. ”MARTA (Muon Auger RPC for the Tank Array) Design Report”. Auger internal note: GAP-2013-020, 2013.

[20] FZU IFSC/USP LIP et al, CBPF. ”MARTA (Muon Auger RPC for the Tank Array) 1st progress report”. Auger internal note: GAP-2013-052, 2013.

[21] E. Lorenz and D. Renker. ”Advances in solid state photon detectors”. *Journal of Instrumentation*, 4, 2009. P04004.

[22] J. Rennefeld and A. Stahl. Studien zur Eignung von Silizium Photomultiplieren für den Einsatz im erweiterten CMS Detektor am SLHC. Masterarbeit, RWTH Aachen University, 2010.

[23] Saint-Gobain Crystals. Premium plastic scintillators. Brochure. 2005.

[24] T. Hebbeker et al. ”Muon measurement using scintillator tiles with SiPM readout”. Auger internal GAP note: GAP-2013-057, 2013.

[25] Saint-Gobain Crystals. Scintillating optical fibers. Brochure. 2005.

[26] Particle Data Group. ”Passage of particles through matters”. 2011. Taken from: http://www-pdg.lbl.gov/2011/reviews/rpp2011-rev-passage-particles-matter.pdf (Access: 27.9.2014 14:00).

[27] S. Agostinelli et al. ”GEANT 4 - a simulation toolkit”. NIM Section A, Volume 506, Section 3, 2003.

[28] T. Niggemann et al. ”A generic Geant4 simulation toolkit for silicon photomultipliers”. https://forge.physik.rwth-aachen.de/projects/g4sipm.

[29] D. Heck et al. ”CORSIKA: A monte Carlo code to simulate extensive air shower”. Vol. 6019. FZKA, 1998.

[30] Hamamatsu Photonics. Technical Information - MPPC models. Brochure. 2013.

[31] L. Middendorf. Measurements of the EASIROC slow shaper. Internal presentation. 2014.

[32] R. Abbasi et al. ”Measurement of the Flux of Ultrahigh Energy Cosmic Rays from Monocular Observations by the High Resolution Fly’s Eye Experiment”. *Phys. Rev. Lett.*, 92, 2004. DOI: 10.1103.

[33] D. Perkins. *Particle Astrophysics.* Oxford University Press Inc., Oxford, 2003.

Acknowledgements

An dieser Stelle möchte ich mich für die tolle Zeit bedanken, die ich mit der Auger Arbeitsgruppe erleben durfte.

Für die Ermöglichung dieser Arbeit in diesem hochinteressanten und aktuellen Forschungsgebiet bedanke ich mich ganz herzlich bei Herrn Prof. Dr. Hebbeker.

Die gesamte Arbeitsatmosphäre empfand ich als sehr angenehm. Ein dankeschön gilt den vielen netten Persönlichkeiten, die ich während meiner Arbeit kennenlernen durfte und die allesamt sehr hilfsbereit waren. Ein ganz besonderes Dankeschön gilt dabei meiner Betreuerin Christine Peters die keine Mühen gescheut hat um mir zu helfen und die Arbeit zur Kontrolle gleich mehrfach gelesen hat. Ebenfalls bedanke ich mich bei Tim Niggemann und Lukas Middendorf die mich ebenfalls unterstützt haben und die Arbeit kontrollgelesen haben.
Für die angenehme Arbeitsatmosphäre im Büro möchte ich mich ebenfalls bei Franziska Knuth und Dominik Sommer bedanken.

Weiterhin gilt mein Dank Patrick Ziegler und Felix Frank für das Lesen dieser Arbeit und ihren Anregungen.

Zu guter letzt darf selbstverständlich auch nicht die mentale Unterstützung von Familie, Freunden und Freundin in der Heimat vergessen werden!

Erklärung

Hiermit versichere ich, dass ich diese Arbeit einschließlich beigefügter Zeichnungen, Darstellungen und Tabellen selbstständig angefertigt und keine anderen als die angegebenen Hilfsmittel und Quellen verwendet habe. Alle Stellen, die dem Wortlaut oder dem Sinn nach anderen Werken entnommen sind, habe ich in jedem einzelnen Fall unter genauer Angabe der Quelle deutlich als Entlehnung kenntlich gemacht.

Aachen, 30. September 2014

Marcus Wirtz